EUROPEAN ORGANIZATION FOR NUCLEAR RESEARCH (CERN)

CERN-EP-2023-004
2023/03/02

CMS-HIG-21-007

A search for decays of the Higgs boson to invisible particles in events with a top-antitop quark pair or a vector boson in proton-proton collisions at $\sqrt{s} = 13\,\text{TeV}$

The CMS Collaboration

Abstract

A search for decays to invisible particles of Higgs bosons produced in association with a top-antitop quark pair or a vector boson, which both decay to a fully hadronic final state, has been performed using proton-proton collision data collected at $\sqrt{s} = 13\,\text{TeV}$ by the CMS experiment at the LHC, corresponding to an integrated luminosity of $138\,\text{fb}^{-1}$. The 95% confidence level upper limit set on the branching fraction of the 125 GeV Higgs boson to invisible particles, $\mathcal{B}(\text{H} \to \text{inv})$, is 0.47 (0.40 expected), assuming standard model production cross sections. The results of this analysis are combined with previous $\mathcal{B}(\text{H} \to \text{inv})$ searches carried out at $\sqrt{s} = 7$, 8, and 13 TeV in complementary production modes. The combined upper limit at 95% confidence level on $\mathcal{B}(\text{H} \to \text{inv})$ is 0.15 (0.08 expected).

Submitted to the European Physical Journal C

1 Introduction

The Higgs boson (H) [1–6] of mass 125 GeV was discovered by the ATLAS and CMS Collaborations in 2012 [7–9]. Since then its properties, including its coupling to other standard model (SM) particles, have been extensively studied using proton-proton (pp) collision data from the CERN LHC collected at $\sqrt{s} = 7$, 8, and 13 TeV with the ATLAS [10] and CMS [11] detectors. Properties of the Higgs boson can be exploited to probe for signs of behaviour beyond the SM (BSM). In the SM, the decay of the Higgs boson to an invisible final state ($H \to \text{inv}$) is only possible via $H \to ZZ^* \to 4\nu$, with a branching fraction of 0.1% [12]. Several BSM theories predict a larger branching fraction to invisible final states, $\mathcal{B}(H \to \text{inv})$ [13–16], namely in Ref. [17] and references therein. For example, in a scenario where the Higgs boson connects the SM and dark matter (DM) sectors [18–23], $\mathcal{B}(H \to \text{inv})$ is enhanced as the Higgs boson can decay to a pair of DM particles of mass $m_{\text{DM}} < m_{\text{H}}/2$.

Direct searches for $H \to \text{inv}$ have been performed by the ATLAS [24–28] and CMS [29–34] Collaborations using data collected during Run 1 (2011–2012) and Run 2 (2015–2018). These target channels in which the Higgs boson is produced via vector boson fusion (VBF), gluon-gluon fusion (ggH), and in association with either a vector boson (VH, where V stands for either a W or Z boson) or with a $t\bar{t}$ quark pair ($t\bar{t}H$). The current most stringent constraint on $\mathcal{B}(H \to \text{inv})$ set by the CMS experiment is via the VBF channel using Run 1 and Run 2 data, which reports a 95% confidence level (CL) upper limit of 0.18 (0.10 expected) [34].

In this paper, a search for an invisibly decaying Higgs boson, produced in association with a $t\bar{t}$ quark pair or a V boson, where the associated particles decay to a fully hadronic final state, is reported. Representative leading order (LO) Feynman diagrams for $t\bar{t}H$ and VH are presented in Fig. 1. The search in the VH channel looks only at topologies in which the presence of the V boson is inferred from well separated decay products, complementing the previous VH search with merged decay products arising from boosted V bosons [33]. The search uses LHC pp collision data collected during the years 2016–2018, corresponding to a total integrated luminosity of 138 fb^{-1} at $\sqrt{s} = 13$ TeV. This is the first search for hadronic final states of $t\bar{t}H$ in a $H \to \text{inv}$ analysis using CMS data, and the first for resolved VH topologies using this data.

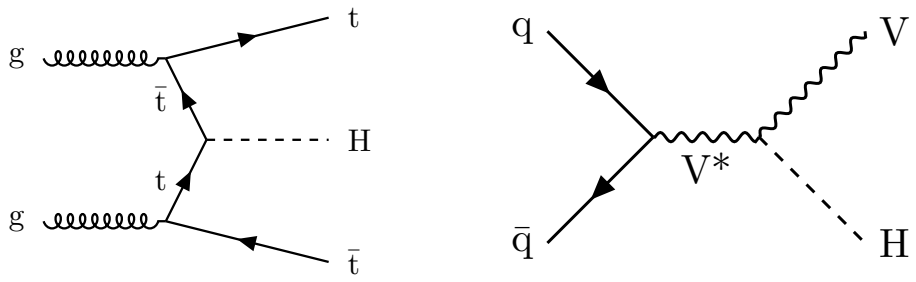

Figure 1: Representative LO Feynman diagrams for the SM Higgs boson production channels $t\bar{t}H$ and VH.

Missing transverse momentum, $\vec{p}_{\text{T}}^{\text{miss}}$, is the transverse component of the negative vector sum of all reconstructed particle momenta in an event, and its magnitude, $p_{\text{T}}^{\text{miss}}$, is used as the discriminating variable to separate the $H \to \text{inv}$ signal from backgrounds. There are two main sources of background affecting the $p_{\text{T}}^{\text{miss}}$ measurement. The first is events with invisible Z boson decays and visible jets ($Z \to \text{inv}$). The second, referred to as the lost lepton background, ℓ_{lost} where ℓ stands for either an e or μ, includes events from $t\bar{t}$ + jets and W + jets production processes where one or more leptons are misreconstructed, excluded by the phase

space selection, or fall outside the detector acceptance. Control regions (CRs) enriched in these background sources, requiring either one lepton, one photon, or two same-flavour opposite-sign leptons, are used to constrain these backgrounds from data. The 95% CL upper limit on $\mathcal{B}(\mathrm{H} \to \mathrm{inv})$ is extracted from a fit to the hadronic recoil distribution of selected events, performed across the signal regions (SRs) and CRs. The hadronic recoil is defined as the $p_{\mathrm{T}}^{\mathrm{miss}}$ of an event excluding the transverse momentum, $\vec{p}_{\mathrm{T}}$, of any identified charged leptons or photons. In the SRs, the hadronic recoil is equivalent to the $p_{\mathrm{T}}^{\mathrm{miss}}$ while in the CRs it effectively measures the p_{T} of the V boson or photon. The exclusion of leptons and photons ensures good correspondence between SRs and CRs.

This paper is organised as follows: Section 2 is a brief description of the CMS detector. The simulated samples used in this analysis are summarised in Section 3. Section 4 describes the event reconstruction and object definitions used in this analysis, while the event selection and event categorisation are detailed in Section 5. The data CRs used for estimating the SM backgrounds are introduced in Section 6. Section 7 describes the statistical procedure used to constrain the backgrounds and extract the signal. The results of the search are presented in Section 8. The results of combining this search with other CMS searches for invisibly decaying Higgs bosons are described in Section 9, and the results are summarised in Section 10.

2 The CMS detector

The CMS apparatus is a multipurpose, nearly hermetic detector, designed to trigger on [35, 36] and identify electrons, muons, photons, and (charged and neutral) hadrons [37–39]. The central feature of the CMS apparatus is a superconducting solenoid, of 6 m internal diameter. Within the field volume are the silicon pixel and strip tracker, the crystal electromagnetic calorimeter (ECAL), and the brass-scintillator hadron calorimeter (HCAL). Muons are measured in gas-ionisation chambers embedded in the steel flux-return yoke of the magnet. Besides the barrel and endcap detectors, CMS has extensive forward calorimetry, performed on high η objects in the HCAL forward calorimeter, which is located 11.2 m from the interaction region along the beam axis. A global "particle-flow" (PF) algorithm [40] aims to reconstruct all individual particles in an event, combining information provided by all subdetectors. The reconstructed particles are used to build τ leptons, jets, and $p_{\mathrm{T}}^{\mathrm{miss}}$ [41–43].

The first level of the CMS trigger system, composed of custom hardware processors, uses information from the calorimeters and muon detectors to select the most interesting events, at a rate of roughly 100 kHz. The high-level trigger (HLT) processor farm performs event reconstruction similar to that of the full CMS reconstruction, but optimised for speed. This decreases the event rate from around 100 kHz to around 1 kHz, before data storage [36].

The procedures for calculating the integrated luminosity recorded by the CMS detector for each data-taking year are documented in Refs. [44–46] for 2016–2018, respectively.

A more detailed description of the CMS experiment can be found in Ref. [47].

3 Simulated samples

Monte Carlo (MC) simulated events are used to model signal and background contributions in all analysis regions, except for quantum chromodynamics (QCD) multijet production processes, which are estimated from data using a dedicated control sample and simulation-based transfer factors. The method for estimating QCD multijet production is detailed in Section 6.2. In all cases, MC samples are produced using either POWHEG version 1.0 or higher [48] or MAD-

GRAPH5_aMC@NLO version 2.4.2 or higher [49] matrix element (ME) generators. The ME is encoded with the maximum amount of information available for a hard scattering event. The parton-level simulation provided by the ME generators is interfaced with PYTHIA version 8 [50] to model the shower and hadronisation of partons in the initial and final states, along with the underlying event description, using the tune CUETP8M1 (CP5) when simulating events for the 2016 (2017 and 2018) data-taking periods [51]. The propagation of all final state particles through the CMS detector is simulated using the GEANT4 [52] toolkit. Samples for 2016 make use of the NNPDF3.0 LO or next-to-LO (NLO) parton distribution functions (PDFs) [53], whereas samples for the years 2017 and 2018 use the NNPDF3.1 next-to-NLO (NNLO) PDFs.

Processes featuring $H \to$ inv occurring in $t\bar{t}H$, VH, VBF, and ggH channels are modelled by POWHEG version 2.0 [54–57] at NLO in QCD. These samples require the SM Higgs boson to decay to four neutrinos ($H \to ZZ^* \to 4\nu$) resulting in $\mathcal{B}(H \to \text{inv}) = 1$. The cross sections are appropriately normalised to the corresponding SM predictions computed at NLO ($t\bar{t}H$), NNLO (VH, VBF), and next-to-NNLO (ggH) accuracy in QCD, and to NLO accuracy in electroweak (EW) corrections [58]. Background ZH processes with the Higgs boson decaying to $b\bar{b}$ and the associated Z boson decaying to $b\bar{b}$, $\ell\ell$, and $q\bar{q}$ (where q represents a light or charm quark) are generated at NLO using MADGRAPH5_aMC@NLO with the FxFx [59] matching scheme for 2016 samples, and with POWHEG version 2.0 [60] for 2017 and 2018 samples.

The V + jets processes are generated at LO in QCD using MADGRAPH5_aMC@NLO with up to four partons in the final state using the MLM [61] matching scheme between hard scatters and parton showers. These processes are generated in bins of hadronic transverse energy, H_T, which is the magnitude of the $\vec{p}_T$ sum of all jets reconstructed at generator level. The LO simulation of V + jets processes is corrected to account for missing higher-order diagrams with K-factors derived from MADGRAPH5_aMC@NLO-generated NLO QCD V + jets processes with up to two partons. These K-factors are extracted as a function of boson p_T and the p_T of the leading jet in the event.

The γ + jets processes are generated at NLO in QCD with MADGRAPH5_aMC@NLO, using a binning based on the p_T of the photon. The binning scheme for this sample is defined at the ME level to increase the statistical precision in the phase space regions probed by this analysis.

Processes including t-channel single t quarks, and $t\bar{t}$ pairs with up to two additional partons in ME computation are generated at NLO with POWHEG version 2.0 [62, 63]. Single t quarks produced in the s-channel are modelled using MADGRAPH5_aMC@NLO, and also in the tW channel using POWHEG version 1.0 [64]. The t quark p_T spectrum in $t\bar{t}$ processes is corrected to match the spectrum obtained from the NNLO QCD + NLO EW simulation, following Ref. [65]. Rare $t\bar{t}X$ + jets backgrounds cover processes where $t\bar{t}$ is produced in association with a boson X (γ, V, or a visibly decaying H), generated at NLO. The $t\bar{t}\gamma$ + jets, $t\bar{t}W$ + jets, and $t\bar{t}Z$ + jets samples are generated using MADGRAPH5_aMC@NLO, with subsequent decays generated using MADSPIN [66] to account for spin correlations in the former two cases. The $t\bar{t}H$ + jets sample, where the H decays to visible states, is generated using POWHEG.

Diboson ZZ and WZ production processes are generated at LO using PYTHIA, while the WW process is simulated at NLO in QCD using the POWHEG version 2.0 [67]. The QCD multijet samples are generated at LO using MADGRAPH5_aMC@NLO in exclusive ranges of H_T in order to increase the statistical precision in the phase-space probed by this analysis.

4 Event reconstruction

During LHC runs, each beam crossing results in several pp collisions in the detector. Additional pp interactions within the same or nearby bunch crossing, known as pileup, make PF object reconstruction more challenging. The reduction of the effect of pileup relies on mitigation techniques [68] that filter energy deposits associated with pileup vertices and remove objects not associated with the primary interaction vertex (PV). The PV is the vertex associated with the hardest scattering in the event, according to tracking information, as described in Ref. [69]. All simulated samples from Section 3 are reweighted to match the pileup distribution observed in data. In the SR, the final state is required to contain jets, a sizeable hadronic recoil, and no isolated leptons or photons. Candidate leptons and photons are selected with $p_{\mathrm{T}} > 10\,\mathrm{GeV}$ and pseudorapidity $|\eta| < 2.4$ for muons [38], $p_{\mathrm{T}} > 10\,\mathrm{GeV}$ and either $|\eta| < 1.44$ or $1.57 < |\eta| < 2.5$ for electrons [37], $p_{\mathrm{T}} > 20\,\mathrm{GeV}$ and $|\eta| < 2.3$ for hadronically decaying tau leptons [41], and $p_{\mathrm{T}} > 15\,\mathrm{GeV}$ and either $|\eta| < 1.44$ or $1.57 < |\eta| < 2.5$ for photons [37]. These selection criteria are optimised to reject reducible background contributions, and other criteria, which depend on the isolation of a given object (lepton or photon) relative to other PF particles within a cone of small (tight) or large (loose) radius, are used to select leptons and photons. Loose identification and isolation criteria are used to veto candidate events in the SR that contain leptons or photons. The veto efficiencies are >99, ≃95, and ≃90% for loose muons, electrons, and photons, respectively. The SR background contributions are estimated using $\mu +$ jets, $\mathrm{e} +$ jets, $\mu\mu +$ jets, $\mathrm{ee} +$ jets, and $\gamma +$ jets. Tight and loose identification and isolation criteria are used to select and count muons, electrons, and photons in the CRs, enhancing the purity at little expense to the efficiency. These achieve typical selection efficiencies of ≃95, 70, and 70 (≃98, 95 and 90)%, for tight (loose) muons, electrons, and photons, respectively.

Jets are reconstructed by clustering all PF candidates originating from the PV with the anti-k_{T} jet clustering algorithm [70, 71], using a distance parameter $R = 0.4$ (AK4). Jet momentum is determined as the vectorial sum of all particle momenta in the jet, and is found from simulation to be, on average, within 5 to 10% of the true momentum over the whole p_{T} spectrum and detector acceptance. Charged-hadron subtraction [42] is then applied to remove charged particles from pileup vertices [72]. To ensure the measured jet energy matches that of the particle level jets, jet energy corrections (JEC) derived from simulation as functions of p_{T} and η are applied. Further corrections are applied due to residual discrepancies in the jet energy scale (JES) between data and simulated samples [42]. Additionally, each jet must pass selection criteria to remove jets adversely affected by instrumentation or reconstruction failure. The jet energy resolution (JER) in simulated samples is smeared to match the measured resolution, which is typically 15–20% at 30 GeV, 10% at 100 GeV, and 5% at 1 TeV [42]. The AK4 jets are required to have $p_{\mathrm{T}} > 30\,\mathrm{GeV}$ and $|\eta| < 5.0$, and those with loose leptons and photons located within a cone of $\Delta R < 0.4$ of the jet direction are removed.

The AK4 jets that originate from the hadronisation of a bottom quark (b-tagged jets) are identified using the DEEPCSV algorithm, which correctly identifies b jets with $p_{\mathrm{T}} > 20\,\mathrm{GeV}$ with a probability of 80% and has a charm or light jet mistag probability of 10% [73]. Simulated events containing b jets are corrected to be in agreement with the data by deriving corrections from data control samples that contain b jets.

Pileup effects are mitigated at the reconstructed particle level using the pileup per particle identification algorithm (PUPPI) [74, 75] by defining a local shape variable that can discriminate between particles originating from the PV and from pileup. Charged particles originating from pileup are discarded. For neutral particles, a local shape variable is computed based on the information from charged particles in their vicinity that originate from the PV within the

tracker acceptance, and information from both charged and neutral particles outside this acceptance. The momenta of neutral particles are then rescaled based on the probability that they originated from the PV as deduced from the local shape variable [74].

When a high p_T t quark or V boson decays hadronically, a large set of collimated particles cross the detector. These can be clustered within a single jet of radius $R = 0.8$ (AK8) using the anti-k_T algorithm. In order to reduce pileup effects, PUPPI PF candidates are used to seed the AK8 jet finder. The main feature that distinguishes hadronically decaying t quarks or V bosons from the quark or gluon fragmentation is the jet mass. To improve the resolution, the modified mass-drop tagger algorithm [76–78] (also known as the soft-drop algorithm, SD) with the angular exponent $\beta = 0$, soft cutoff threshold $z_{cut} < 0.1$, and characteristic radius $R_0 = 0.8$ [79] is applied to each AK8 jet to remove soft and wide-angle radiation. In addition, a deep neural network (DNN) classifier called the DEEPAK8 [80] algorithm is employed by assigning a set of numerical scores to each reconstructed AK8 jet corresponding to the probabilities that it originates from particular final states of V boson decays, for example $Z \to b\bar{b}$, $Z \to q\bar{q}$, $W \to cs$, rather than from QCD multijet processes. For this analysis, reconstructed AK8 jets originating from t quarks (W bosons) are selected by requiring $p_T > 400$ (200) GeV, SD mass m_{SD} between 120 and 210 (65 and 120) GeV, and a DeepAK8 probability score for t quarks (W bosons) larger than between 72.5 and 83.4 (91.8 and 92.5)% depending on the year of data-taking. The resulting t quark (W boson) tagging efficiency at the $p_T > 400$ (200) GeV threshold limit is estimated from simulation as 28 (25)% with a 1% mistag rate from QCD jets. Simulated events containing AK8 jets are corrected to agree with the data using data-derived correction factors, and dedicated JEC are also applied [80].

The calculation of energy sums such as the hadronic recoil, $\vec{p}_T^{\,miss}$, and $\vec{H}_T^{miss}$ are based on AK4 jets, therefore JEC are propagated through the use of the $\vec{p}_T$-corrected jets.

5 Event selection and categorisation

In this analysis the signal is extracted from a fit to the hadronic recoil distribution of events in the SR. The CRs are used to estimate the contributions of different SM processes in the SR. Where possible, the CRs have kinematic requirements identical to the SR, and leptons or a photon are used in the CR definition, but otherwise ignored in the calculation of event observables. The e + jets and μ + jets CRs, enriched in W + jets and t quark background processes, are used to derive corrections to the irreducible ℓ_{lost} backgrounds predicted by simulation. The ee + jets, $\mu\mu$ + jets, and, in the case of the VH category, γ + jets CR samples are used to derive corrections to the expected contribution from Z + jets production, where the Z boson decays to a pair of neutrinos. A QCD multijet enriched CR (hadronic sideband) is also used to estimate reducible hadronic backgrounds in the SR.

5.1 Trigger requirements

Events of interest are collected via a suite of triggers that are applied to variables calculated using PF candidates reconstructed at the level of the HLT. The trigger requirements vary amongst analysis regions and data-taking periods. Events in the SR, hadronic sideband, and muon CRs are collected using HLT selection criteria on p_T^{miss} and the missing H_T, H_T^{miss}, which is the magnitude of the negative $\vec{p}_T$ sum of jets reconstructed at the HLT level with a p_T^{miss} threshold of 20 GeV applied. Muons are not considered in the calculation of PF p_T^{miss} and PF H_T^{miss} to allow the same trigger to be used in the SR and the muon CRs, with a typical efficiency of >90% for $p_T^{miss} > 250$ GeV. The use of the combined p_T^{miss} and H_T^{miss} triggers in the muon CRs instead of single-muon triggers corresponds more closely to the selection in the SR and minimises

selection biases. Trigger thresholds increase with time due to the increase in instantaneous luminosity during Run 2. In 2016, the $p_{\mathrm{T}}^{\mathrm{miss}}$ and $H_{\mathrm{T}}^{\mathrm{miss}}$ thresholds vary between 90 and 120. In 2017 and 2018, these thresholds are 120 GeV. During data-taking in 2017, additional corrections were applied to account for the effect of ECAL endcap noise at high $|\eta|$ on PF $p_{\mathrm{T}}^{\mathrm{miss}}$ measurements. Additionally, for 2016 and 2017 data-taking periods, there was an inefficiency arising from a gradual shift in the timing of the ECAL trigger inputs in the region $|\eta| > 2.0$ [35]. This resulted in events containing an electron or photon (jet) with $p_{\mathrm{T}} > 50$ (100) GeV having an efficiency loss of up to 20%, depending on p_{T} and η. Correction factors for this trigger inefficiency are obtained from 2016 and 2017 data and applied to simulation samples as a function of η.

Events in the e + jets and ee + jets CRs from the 2016, 2017, and 2018 data sets are required to pass a tight (loose) single-electron trigger with p_{T} thresholds of 27, 35, and 32 (105, 115, and 115) GeV, respectively. The low-threshold single-electron triggers require the electron candidate to pass a tight isolation condition, while the high-threshold trigger imposes a looser selection on the isolation to improve the efficiency at high p_{T}. Photon events are required to pass a single-photon trigger with a p_{T} threshold of 175 (200) GeV without any isolation condition for the 2016 (2017 and 2018) data sets. Simulated electron or photon events are accepted if they pass exactly one of the above trigger requirements, and the efficiency of this selection is corrected with data-derived efficiency correction factors.

5.2 Offline selection

In order to select events with a large amount of jet activity and sizeable hadronic recoil, a further offline selection is applied to all regions. To improve the purity of the signal, large missing energy is desirable, therefore events require $p_{\mathrm{T}}^{\mathrm{miss}}$, $H_{\mathrm{T}}^{\mathrm{miss}}$, and H_{T} to be greater than 200 GeV. Furthermore, the largest p_{T} of an AK4 jet in an event, $\vec{p}_{\mathrm{T},1}^{\,\mathrm{j}}$, is required to be greater than 80 GeV. Agreement between the hadronic recoil and $H_{\mathrm{T}}^{\mathrm{miss}}$ is ensured by requiring $H_{\mathrm{T}}^{\mathrm{miss}}/p_{\mathrm{T}}^{\mathrm{miss}} < 1.2$ and azimuthal separation $|\Delta\phi(\vec{p}_{\mathrm{T}}^{\mathrm{miss}}, \vec{H}_{\mathrm{T}}^{\mathrm{miss}})| < 0.5$. To ensure good correspondence between $p_{\mathrm{T}}^{\mathrm{miss}}$ as measured including and excluding charged lepton PF candidates in both the SR and the hadronic sideband, a selection is made on $p_{\mathrm{T,track}}^{\mathrm{miss}}$, which is equivalent to $p_{\mathrm{T}}^{\mathrm{miss}}$ but calculated using only charged PF particles. Requirements of $p_{\mathrm{T,track}}^{\mathrm{miss}} > 60$ GeV and azimuthal separation to the recoil direction $|\Delta\phi(\text{recoil}, \vec{p}_{\mathrm{T,track}}^{\mathrm{miss}})| < 1$ are applied. The kinematic selection for all regions is optimised according to the Asimov significance between signal (S) and background (B) yields assuming a background systematic uncertainty ΔB of 5% or 10% [81]. The peaks of the distribution for a given variable corresponds to its selection threshold.

In order to facilitate the combination of this analysis with the results from other H $\rightarrow$ inv searches, additional selections are introduced to reduce the potential event overlap. A veto is implemented to ensure orthogonality with the VBF phase space, through a veto on events with leading (subleading) AK4 jets with $|\eta_1|$ ($|\eta_2|$) > 2.4, and an inversion of the kinematic selection employed by the VBF H $\rightarrow$ inv analysis [34]. This removes events containing two AK4 jets with $\vec{p}_{\mathrm{T},1}^{\,\mathrm{j}} > 80$ GeV and the subleading jet p_{T}, $\vec{p}_{\mathrm{T},2}^{\,\mathrm{j}}$, to be greater than 40 GeV, where the jets are from opposite detector hemispheres ($\eta_1\eta_2 < 0$), have a large m_{jj} (>200 GeV), small azimuthal separation ($\Delta\phi_{\mathrm{jj}} < 1.5$), and a large η gap ($|\eta_{m_{\mathrm{jj}}}| > 1.0$). Moreover, orthogonality to leptonic $\mathrm{t\bar{t}H}$ decays is ensured in the single-lepton CRs by requiring the transverse mass of the combined single-lepton and $\vec{p}_{\mathrm{T}}^{\mathrm{miss}}$ system, defined as

$$m_{\mathrm{T}}^{\ell} = \sqrt{2p_{\mathrm{T}}^{\ell}p_{\mathrm{T}}^{\mathrm{miss}}[1 - \cos(\phi(\vec{p}_{\mathrm{T}}^{\ell}) - \phi(\vec{p}_{\mathrm{T}}^{\mathrm{miss}}))]}, \tag{1}$$

to be lower than 110 GeV. Orthogonality between leptonic $\mathrm{t\bar{t}H}$ decays in the dilepton CRs is ensured by requiring the invariant mass of the charged lepton pair, $m_{\ell\ell}$, to be lower than

120 GeV in these CRs. Selecting on the invariant masses of lepton pairs also suppresses the $t\bar{t}H$ signal contamination in the CRs. Overlap between the ggH/boosted VH $H \to$ inv analysis and the resolved VH category of this analysis is rendered negligible by explicitly removing events from the low-purity boosted VH category defined in Ref. [33] if they contain exactly two AK4 jets with an invariant mass, m_{jj}, forming a dijet candidate with $65 < m_{jj} < 120$ GeV. No corresponding selection is necessary for the resolved VH category as a result, while there is negligible change to the sensitivity of the boosted VH category.

During significant periods of data-taking in 2018, the HCAL portion corresponding to the region $-1.57 < \phi < -0.87$, $-3.0 < \eta < -1.39$ was not functional. Events from 2018 with $-1.8 < \phi(\vec{p}_T^{\,miss}) < -0.6$ are vetoed if they contain jets within the affected region, which removes ≈65% of the total data from the affected region. To ensure good correspondence between data and simulation, the simulation is reweighted to account for the efficiency loss. A summary of the offline requirements are provided in Table 1.

Table 1: Offline selection applied to all categories and regions in this analysis to improve signal purity and reduce overlap with the phase space of other $H \to$ inv searches.

Variable	Selection	Purpose
p_T^{miss}	> 200 GeV	Signal purity
H_T^{miss}	> 200 GeV	
$\vec{p}_{T,1}^{\,j}$	> 80 GeV	
H_T^{miss} / p_T^{miss}	< 1.2	Event quality
$\lvert\Delta\phi(\vec{p}_T^{\,miss}, \vec{H}_T^{miss})\rvert$	< 0.5	
$\lvert\eta_1\rvert$, $\lvert\eta_2\rvert$	< 2.4	Analysis orthogonalisation
VBF signal	Veto (inversion on signal selection)	
m_T^{ℓ}	< 110 GeV	
$m_{\ell\ell}$	< 120 GeV	

5.3 Signal regions

The search focuses on three types of hadronic final states: those with boosted t quarks and/or boosted W bosons reconstructed with dedicated merged jet algorithms; those with at least five AK4 jets and one or more b jets and no boosted t quark or W boson, targetting the bulk of hadronic $t\bar{t}H$ events; and those with two resolved jets with the m_{jj} compatible with that of a W or Z boson. The latter complements the boosted VH channel analysed in Ref. [33].

Events are categorised into boosted and resolved $t\bar{t}H$, and resolved VH topologies. The $t\bar{t}H$ category requires that at least five AK4 jets and one b jet are present. The boosted $t\bar{t}H$ topology requires that at least one AK8 jet is reconstructed and either t- or W-tagged, and is subcategorised by the AK8 jet and b jet multiplicities. Events without such t- or W-tagged jets are categorised as belonging to a resolved $t\bar{t}H$ topology, with further selections on the leading AK4 jet (leading or subleading b jet) $\vec{p}_T$ and $\vec{p}_T^{\,miss}$, $|\Delta\phi(\vec{p}_T^{\,miss}, \vec{p}_{T,1}^{\,j})|$ ($|\Delta\phi(\vec{p}_T^{\,miss}, \vec{p}_{T,1}^{\,b})|$ or $|\Delta\phi(\vec{p}_T^{\,miss}, \vec{p}_{T,2}^{\,b})|$) applied to discriminate between $t\bar{t}H$ and $t\bar{t}$ + jets processes. Finally, the remaining events are allocated to the resolved VH topology category if they have exactly two AK4 jets with m_{jj} between 65 and 120 GeV, compatible with a W or Z boson decay. The resolved VH subcategories are separated according to the b jet multiplicity. Subcategories are also defined based on $\vec{p}_{T,2}^{\,j}$ to suppress QCD multijet background. The subcategory definitions are summarised in Table 2. The intended outcome of this categorisation is a set of event samples with high purity for a given production mode, and minimal background contamination or signal cross-

contamination.

Table 2: Categorisation of the $t\bar{t}H$ and VH production modes in the analysis. No additional selections are applied to the boosted $t\bar{t}H$ subcategories.

Category	Subcategory	n_j	n_b	n_t	n_W	$\vec{p}_{T,2}^{\,j}$ (GeV)	Other
Boosted $t\bar{t}H$	2Boosted1b	≥ 5	1		2	> 80	—
	2Boosted2b	≥ 5	≥ 2		2		
	1t1b	≥ 5	1	1	0		
	1t2b	≥ 5	≥ 2	1	0		
	1W1b	≥ 5	1	0	1		
	1W2b	≥ 5	≥ 2	0	1		
Resolved $t\bar{t}H$	5j1b	5	1	0	0	> 80	$\lvert\Delta\phi(\vec{p}_T^{\,miss}, \vec{p}_{T,1}^{\,b})\rvert > 1.0$, $\lvert\Delta\phi(\vec{p}_T^{\,miss}, \vec{p}_{T,1}^{\,j})\rvert > \pi/2$
	6j1b	≥ 6	1	0	0		
	5j2b	5	≥ 2	0	0		$\lvert\Delta\phi(\vec{p}_T^{\,miss}, \vec{p}_{T,1}^{\,b})\rvert > 1.0$, $\lvert\Delta\phi(\vec{p}_T^{\,miss}, \vec{p}_{T,2}^{\,b})\rvert > \pi/2$
	6j2b	≥ 6	≥ 2	0	0		
VH	2j0b	2	0	0	0	> 30	$65 < m_{jj} < 120\,\text{GeV}$
	2j1b	2	1	0	0		
	2j2b	2	2	0	0		

A requirement on $|\Delta\phi_{min}(\vec{p}_T^{\,miss}, \vec{p}_{T,1234})|$, defined as the minimum azimuthal separation between $\vec{p}_T^{\,miss}$ and the momentum direction of any of the four highest p_T jets, of > 0.5 is applied to suppress QCD multijet events where the $\vec{p}_T^{\,miss}$ is aligned with a jet. A parameter $\tilde{\omega}_{min}$ is designed to suppress events where missing energy is the result of a jet p_T mismeasurement, and is especially effective in categories with no b jets. This is particularly relevant in the VH 2j0b subcategory, where the QCD multijet contribution can be as much as 15% of the total background after applying the $|\Delta\phi_{min}(\vec{p}_T^{\,miss}, \vec{p}_{T,1234})|$ selection. For the ith jet in the event, ω_i is defined as $\arctan(H_{T,min}^{miss}/p_{T,i})$, where $p_{T,i}$ is the p_T of jet i and $H_{T,min}^{miss}$ is the minimum value of H_T^{miss} that can be obtained by scaling $p_{T,i}$ by a constant factor. The value of ω_i minimised over i is $\tilde{\omega}_{min}$. A detailed derivation of this variable is given in Ref. [82]. QCD multijet events in the SR are further suppressed by requiring $\tilde{\omega}_{min} > 0.3$. Requirements to suppress QCD events are applied in the SR only for $t\bar{t}H$ categories, and to both SR and CRs in the VH categories in order to ensure good correspondence amongst the regions. The selections applied to $\tilde{\omega}_{min}$ and $|\Delta\phi_{min}(\vec{p}_T^{\,miss}, \vec{p}_{T,1234})|$ are not applied in the CRs used for background estimation of the $t\bar{t}H$ categories, where p_T^{miss} does not stem from jet mismeasurement. This is to increase event counts in the CRs, particularly in the boosted $t\bar{t}H$ categories.

The $\vec{p}_T^{\,miss}$ in $t\bar{t}H$ production is closely aligned with the direction of the Higgs boson typically. In $t\bar{t}$ events, the p_T^{miss} direction is usually parallel or antiparallel to the direction of the leading b jet, as the t quarks are produced back-to-back. Therefore, the angles between the $\vec{p}_T^{\,miss}$ and the leading or subleading jet or b jet $\vec{p}_T$ directions provide additional features for $t\bar{t}$ background suppression in the resolved $t\bar{t}H$ categories. The angular variables $|\Delta\phi(\vec{p}_T^{\,miss}, \vec{p}_{T,1}^{\,j})|$, $|\Delta\phi(\vec{p}_T^{\,miss}, \vec{p}_{T,1}^{\,b})|$, and $|\Delta\phi(\vec{p}_T^{\,miss}, \vec{p}_{T,2}^{\,b})|$ are the most sensitive discriminators between $t\bar{t}H$ and $t\bar{t}$. The selection based on these angular variables has been optimised by maximising the combined expected sensitivity of the $t\bar{t}H$ analysis and is summarised in Table 2.

6 Control regions and background estimation

The analysis makes use of the μ + jets and e + jets CRs to estimate irreducible background contributions due to ℓ_{lost}, which are mainly from $\mathrm{t\bar{t}}$ + jets, single t quark, and W + jets events. The irreducible background contributions from invisible Z boson decays, which include ZZ and $\mathrm{t\bar{t}Z}$ and Drell-Yan (DY) contributions, are estimated from the $\mu\mu$ + jets, ee + jets, and γ + jets CRs. Reducible hadronic backgrounds in the SR such as QCD multijet contributions are estimated using a transfer factor method applied to a QCD enriched sideband CR.

6.1 Irreducible background estimation

The μ + jets (e + jets) CR is defined by requiring exactly one tightly-isolated muon (electron) with $p_{\mathrm{T}} > 20(40)$ GeV. Both CRs require $50 < m_{\mathrm{T}}^{\ell} < 110$ GeV. The single-lepton CRs are used to constrain the ℓ_{lost} background, which is the main source of background in the $\mathrm{t\bar{t}H}$ and VH 2j2b categories. In the $\mathrm{t\bar{t}H}$ category, the ℓ_{lost} contribution arises mainly from $\mathrm{t\bar{t}}$, single t quark, and $\mathrm{t\bar{t}V}$ processes, while in the VH category it is from W + jet events.

In the $\mu\mu$ + jets (ee + jets) CR, one tightly-isolated muon (electron) with $p_{\mathrm{T}} > 20$ (40) GeV, and one loose muon (electron) with the opposite charge and $p_{\mathrm{T}} > 10(10)$ GeV are required with invariant mass, $m_{\mu\mu}$ (m_{ee}), compatible with a Z boson. For the $\mathrm{t\bar{t}H}$ (VH) category, the invariant mass is required to be between 75 and 105 (60 and 120) GeV. The processes $\mathrm{Z} \to \nu\overline{\nu}$ and $\mathrm{Z} \to \ell\ell$ are kinematically nearly identical, largely due to lepton universality, hence the dilepton regions can be used to constrain the $\mathrm{Z} \to$ inv background and minimise theoretical uncertainties. This is important for the $\mathrm{Z} \to$ inv background, which dominates the VH category and contributes to the $\mathrm{t\bar{t}H}$ category especially at high hadronic recoil. In the $\mathrm{t\bar{t}H}$ category, events are selected for which $\Delta\phi(\text{recoil}, \vec{p}_{\mathrm{T,track}}^{\,\mathrm{miss}}) > \pi/2$, which reduces the $\mathrm{t\bar{t}}$ + jets background and favours DY production in the dilepton CRs.

The γ + jets CR is used for background estimation in the VH category only, and requires exactly one loose photon with $p_{\mathrm{T}} > 230$ GeV. This region is used to constrain the $\mathrm{Z} \to$ inv background as the event kinematics and topologies are similar for Z + jets and γ + jets events, improving the sensitivity to the VH signal primarily at high hadronic recoil compared to the dilepton CRs because of the larger number of events.

Photons can usually be discriminated from other sources of ECAL deposits using the properties of the deposits themselves, such as isolation in ECAL and HCAL, or the shape of the electromagnetic showers. However, occasionally other particles will be incorrectly identified as photons, for example where a jet is misidentified as a photon in QCD multijet events. In order to estimate the contribution from misidentified photons in the γ + jets CR, a purity measurement is performed. The purity is defined as the fraction of reconstructed photon candidates that correspond to genuine isolated photons originating from the PV in the event. The photon purity is measured in data based on the lateral width $\sigma_{\eta\eta}$ [83], which parametrises the shape of the energy deposit associated with the photon in the ECAL. The characteristic $\sigma_{\eta\eta}$ distribution from genuine photons peaks at $\sigma_{\eta\eta} < 1$, while the distribution due to misidentified photons possesses a less pronounced peak with a much broader decline for $\sigma_{\eta\eta} > 1$. A template fit to the $\sigma_{\eta\eta}$ distribution is performed, where for genuine photons simulated γ + jets events are used to build the signal templates, while for misidentified photons a data sample enriched in misidentified photon events is obtained by inverting the isolation requirements in the γ + jets CR. The purity is defined as the fraction of genuine photons extracted from the fit that pass the $\sigma_{\eta\eta}$ selection. The photon purity is measured separately in bins of p_{T}^{γ} and for each data-taking period. The contamination is the fraction of misidentified photons in the γ + jets CR, and is estimated at around 4% for $p_{\mathrm{T}}^{\gamma} > 200$ GeV. The QCD multijet contribution in the γ + jets CR is then

estimated by weighting events in data for each p_{T}^{γ} bin by the corresponding contamination. A 25% systematic uncertainty is attributed to the QCD multijet background normalisation, and is estimated by performing the procedure for different $\sigma_{\eta\eta}$ binning in the template fit, which accounts for any mismodelling of the simulated $\sigma_{\eta\eta}$ distribution. The statistical uncertainty in the photon purity estimate in each p_{T}^{γ} bin is found to be much smaller than the systematic one. The full requirements for the analysis CRs are shown in Table 3.

Table 3: Summary of all CR requirements, excluding selections suppressing the QCD multijet background, and excluding the requirement of $\Delta\phi(\text{recoil}, \vec{p}_{\mathrm{T,track}}^{\,\mathrm{miss}}) > \pi/2$ applied to the $\mathrm{t\bar{t}H}$ category in the dilepton CRs. No mass requirements are imposed in the $\gamma + \text{jets}$.

Control region	Category	n_{object} reqs.	Mass reqs. (GeV)	p_{T} reqs. (GeV)
$\mu + \text{jets}$	$\mathrm{t\bar{t}H}$ VH	$n_{\mu} = 1$	$50 < m_{\mathrm{T}}^{\mu} < 110$	$p_{\mathrm{T},1}^{\mu} > 20$
$\mathrm{e} + \text{jets}$	$\mathrm{t\bar{t}H}$ VH	$n_{\mathrm{e}} = 1$	$50 < m_{\mathrm{T}}^{\mathrm{e}} < 110$	$p_{\mathrm{T},1}^{\mathrm{e}} > 40$
$\mu\mu + \text{jets}$	$\mathrm{t\bar{t}H}$ VH	$n_{\mu} = 2$	$75 < m_{\mu\mu} < 105$ $60 < m_{\mu\mu} < 120$	$p_{\mathrm{T},1}^{\mu} > 20$, $p_{\mathrm{T},2}^{\mu} > 10$
$\mathrm{ee} + \text{jets}$	$\mathrm{t\bar{t}H}$ VH	$n_{\mathrm{e}} = 2$	$75 < m_{\mathrm{ee}} < 105$ $60 < m_{\mathrm{ee}} < 120$	$p_{\mathrm{T},1}^{\mathrm{e}} > 40$, $p_{\mathrm{T},2}^{\mathrm{e}} > 10$
$\gamma + \text{jets}$	VH	$n_{\gamma} = 1$	—	$p_{\mathrm{T}}^{\gamma} > 230$

6.2 Residual backgrounds from QCD multijet production

The event selection aims to reduce background contributions from QCD multijet production as much as possible by requiring $|\Delta\phi_{\min}(\vec{p}_{\mathrm{T}}^{\,\mathrm{miss}}, \vec{p}_{\mathrm{T,1234}})| > 0.5$ and $\tilde{\omega}_{\min} > 0.3$, although a QCD multijet background enriched sideband is used to estimate any remaining background contribution with the help of a transfer factor between sideband and SR, which is derived from simulation. The sideband is defined with an identical selection to that of the SR, but with an inversion on the requirements on $|\Delta\phi_{\min}(\vec{p}_{\mathrm{T}}^{\,\mathrm{miss}}, \vec{p}_{\mathrm{T,1234}})|$ and $\tilde{\omega}_{\min}$, such that $|\Delta\phi_{\min}(\vec{p}_{\mathrm{T}}^{\,\mathrm{miss}}, \vec{p}_{\mathrm{T,1234}})| < 0.5$ and more stringently $\tilde{\omega}_{\min} < 0.2$. The criteria for $\tilde{\omega}_{\min}$ is determined by optimising the sideband to be as QCD multijet-enriched as possible while ensuring the SR has negligible QCD multijet background. For the VH category, the m_{jj} requirement is also inverted in order to have the sideband sufficiently populated.

The SRs in both the $\mathrm{t\bar{t}H}$ and VH categories suffer from limited simulated QCD multijet event counts, so it is not possible to reliably define a transfer factor for each SR bin in individual subcategories. Within the statistical precision of the simulated QCD multijet samples, the shape of the hadronic recoil and relative population of the $\mathrm{t\bar{t}H}$ subcategories are observed not to depend on $\tilde{\omega}_{\min}$ and $|\Delta\phi_{\min}(\vec{p}_{\mathrm{T}}^{\,\mathrm{miss}}, \vec{p}_{\mathrm{T,1234}})|$. Therefore, the expected QCD sideband yields are integrated over all $\mathrm{t\bar{t}H}$ subcategories and hadronic recoil intervals, and over hadronic recoil intervals for each VH category, in the sideband and SR, to construct the transfer factors. The resulting hadronic recoil distributions are used to predict the relative QCD multijet background in each subcategory and hadronic recoil interval.

The estimated QCD multijet background yield in the $\mathrm{t\bar{t}H}$ SR for subcategory i and hadronic recoil interval j, $N_{i,j}^{\mathrm{QCD,\,SR_{t\bar{t}H}}}$, is given by

$$N_{i,j}^{\mathrm{QCD,\,SR_{t\bar{t}H}}} = \sum_{p}\sum_{q}(N_{p,q}^{\mathrm{data,\,CR_{t\bar{t}H}}} - N_{p,q}^{\mathrm{EW,\,CR_{t\bar{t}H}}})\mathrm{TF}_{\mathrm{QCD}}^{\mathrm{t\bar{t}H}} f_{c_i}^{\mathrm{t\bar{t}H}} f_{m_j}^{\mathrm{t\bar{t}H}}, \tag{2}$$

where EW refers to processes that are not QCD multijet, summation indices p and q are the subcategory and hadronic recoil bins, respectively, $\mathrm{TF}_{\mathrm{QCD}}^{\mathrm{t\bar{t}H}}$ is the QCD multijet simulation transfer factor defined as the ratio between the expected QCD multijet background contribution in the SR and the sideband, and $f_{c_i}^{\mathrm{t\bar{t}H}}$ and $f_{m_j}^{\mathrm{t\bar{t}H}}$ are the fractions of simulated QCD multijet events in each subcategory and hadronic recoil bin, respectively.

In the VH category, the sideband regions are defined for each subcategory, as the number of simulated QCD multijet events is sufficient to derive the hadronic recoil fractions f_{m_j} separately for each subcategory. The method is otherwise analogous to that of $\mathrm{t\bar{t}H}$, given by Eq. 2).

The results of the QCD prediction aggregated over data sets from the 2016–2018 period are found to be small in comparison to background contributions from ℓ_{lost} and $\mathrm{Z} \to \mathrm{inv}$ processes. In addition to the statistical uncertainties, a 100% systematic uncertainty is assigned to the predicted background yields from QCD multijet production. The actual uncertainty in the QCD prediction is measured at around 50%, derived by calculating the QCD contribution in the entire $\mathrm{t\bar{t}H}$ category for a signal depleted validation region analogous to the SR but requiring $0.2 < \tilde{\omega}_{\mathrm{min}} < 0.3$ and $|\Delta\phi_{\mathrm{min}}(\vec{p}_{\mathrm{T}}^{\,\mathrm{miss}}, \vec{p}_{\mathrm{T,1234}})|$, and comparing the estimate to data. It is inflated to 100% to be more conservative when handling the individual $\mathrm{t\bar{t}H}$ subcategories that are limited by event counts at larger hadronic recoil, which was found to have negligible impact on the final fit.

7 Statistical interpretation

A maximum likelihood fit method is used to obtain an upper limit on $\mathcal{B}(\mathrm{H} \to \mathrm{inv})$. The fit is performed simultaneously across each year, region, category, and hadronic recoil interval, with systematic uncertainties acting as nuisance parameters in the fit correlated to varying degrees across year and category.

7.1 Likelihood model

The limits on $\mathcal{B}(\mathrm{H} \to \mathrm{inv})$ are extracted via a simultaneous binned maximum likelihood fit to the hadronic recoil distributions obtained in the SR and CRs. The likelihood can be written as

$$\mathcal{L} = \mathcal{L}_{\mathrm{SR}}\, \mathcal{L}_{\mu}\, \mathcal{L}_{\mathrm{e}}\, \mathcal{L}_{\mu\mu}\, \mathcal{L}_{\mathrm{ee}}\, \mathcal{L}_{\gamma}, \tag{3}$$

where $\mathcal{L}_{\mathrm{SR}}$ is the likelihood function for the SR (boosted $\mathrm{t\bar{t}H}$, resolved $\mathrm{t\bar{t}H}$, VH), and $\mathcal{L}_{\mu}$, $\mathcal{L}_{\mathrm{e}}$, $\mathcal{L}_{\mu\mu}$, $\mathcal{L}_{\mathrm{ee}}$, and $\mathcal{L}_{\gamma}$ designate the likelihood functions for the $\mu+$jets, e$+$jets, $\mu\mu+$jets, ee$+$jets, and $\gamma+$jets CRs, respectively. The likelihood function for the SR is defined as

$$\mathcal{L}_{\mathrm{SR}} = \prod_{\mathrm{cat}=i}^{n_{\mathrm{cat}}} \prod_{\mathrm{recoil}=j(i)}^{n_{\xi(i)}} \mathrm{Poisson}(n_{\mathrm{obs}}^{i,j} \mid n_{\mathrm{pred}}^{i,j}), \tag{4}$$

with

$$\begin{aligned} n_{\mathrm{pred}}^{i,j} = {} & \hat{\mu} s^{i,j} \rho_{s}^{i,j} \\ & + b_{\ell_{\mathrm{lost}}}^{i,j} I^{i,j} \rho_{\ell_{\mathrm{lost}}}^{i,j} \\ & + b_{\mathrm{Z}\to\mathrm{inv}}^{i,j} L^{i,j} \rho_{\mathrm{Z}\to\mathrm{inv}}^{i,j} \\ & + b_{\mathrm{QCD}}^{i,j} \rho_{\mathrm{QCD}}^{i,j}, \end{aligned} \tag{5}$$

where the symbols are defined in Table 4. The signal strength, $\hat{\mu}$, is interpreted as the maximum likelihood estimator for $\mathcal{B}(\mathrm{H} \to \mathrm{inv})$, where the signal prediction assumes that $\mathcal{B}(\mathrm{H} \to \mathrm{inv}) =$

1. The fit also includes additional free parameters $I^{i,j}$ and $L^{i,j}$, which depend on category i, hadronic recoil bin j, and the number of recoil bins in each category $n_{\xi(i)}$. The first of these parameters, $I^{i,j}$, simultaneously scales the normalisation of the ℓ_{lost} background in the SR and the sum of the backgrounds in the μ + jets and e + jets CRs. The second of these parameters, $L^{i,j}$, simultaneously scales the normalisation of the $\text{Z} \to \text{inv}$ background in the SR and the sum of the backgrounds, except the QCD multijet background, in the $\mu\mu$ + jets, ee + jets, and γ + jets CRs.

Table 4: Meaning of the symbols used in Eqs. 4 and 5 that define the likelihood function.

Symbol	Meaning
$\hat{\mu}$	Signal strength estimator of $\mathcal{B}(\text{H} \to \text{inv})$
$s^{i,j}$	Simulation predicted number of signal events in bin i,j of the SR
$\rho_s^{i,j}$	Systematic uncertainties affecting signal prediction in bin i,j of the SR
$b_{\ell_{\text{lost}}}^{i,j}$	Simulation predicted number of ℓ_{lost} events in bin i,j of the SR
$I^{i,j}$	Normalisation parameter for the ℓ_{lost} estimation in bin i,j
$\rho_{\ell_{\text{lost}}}^{i,j}$	Systematic uncertainties affecting the ℓ_{lost} background in bin i,j of the SR
$b_{\text{Z}\to\text{inv}}^{i,j}$	Simulation predicted number of $\text{Z} \to \text{inv}$ events in bin i,j of the SR
$L^{i,j}$	Normalisation parameter for the $\text{Z} \to \text{inv}$ estimation in bin i,j
$\rho_{\text{Z}\to\text{inv}}^{i,j}$	Systematic uncertainties affecting the $\text{Z} \to \text{inv}$ background in bin i,j of the SR
$b_{\text{QCD}}^{i,j}$	Predicted number of QCD events in bin i,j of the SR
$\rho_{\text{QCD}}^{i,j}$	Systematic uncertainties of the QCD component in bin i,j of the SR

The likelihood for each CR is given by

$$\mathcal{L}_{\text{CR X}} = \prod_{\text{cat}=i}^{n_{cat}} \prod_{\text{recoil}=j(i)}^{n_{\xi(i)}} \text{Poisson}(n_{\text{obs}}^{i,j} \mid \text{X}_{\text{bkg}}^{i,j} L^{i,j} \rho_{\text{bkg}}^{i,j}), \tag{6}$$

where $\text{X}_{\text{bkg}}^{i,j}$ is the sum of background yields in CR X, and $\rho_{\text{bkg}}^{i,j}$ refers to the associated systematic uncertainty.

Because of the low event counts in the dilepton CRs, the subcategory yields are summed into the boosted and resolved $\text{t}\bar{\text{t}}\text{H}$ categories. For the boosted $\text{t}\bar{\text{t}}\text{H}$ category, the $\mu\mu$ + jets and ee + jets CR yields are summed together to form a single $\ell\ell$ + jets CR. Furthermore, in the boosted and resolved $\text{t}\bar{\text{t}}\text{H}$ subcategories, $I^{i,j}$ are shared across subcategories, therefore i takes only two values corresponding to the boosted and resolved $\text{t}\bar{\text{t}}\text{H}$ classes.

7.2 Systematic uncertainties

The model on which the maximum likelihood fit is based is inclusive of experimental and theoretical uncertainties. Theoretical uncertainties related to the PDF parameters and missing higher order corrections in the QCD and EW perturbative expansions are estimated by following the procedure outlined in Ref. [58] for $\text{t}\bar{\text{t}}\text{H}$ and VH processes, and in Ref. [84] for V + jets and γ + jets processes.

Data-derived correction factors are applied to simulated events containing b, t, and W jets, and therefore the systematic uncertainties due to the limited precision in these corrections are propagated to the simulated samples. These are referred to as tagging uncertainties, and also account for the uncertainties in the tagging efficiencies and misidentification probabilities.

The uncertainty in the combined $p_{\mathrm{T}}^{\mathrm{miss}}$ and $H_{\mathrm{T}}^{\mathrm{miss}}$ trigger efficiency is computed using the $\mu +$ jets and $\mu\mu +$ jets CRs. These are independent of the $p_{\mathrm{T}}^{\mathrm{miss}}$ and $H_{\mathrm{T}}^{\mathrm{miss}}$ data sets in the SR, ensuring an unbiased measurement of the uncertainty. This uncertainty is measured at 2%. An additional trigger inefficiency uncertainty due to the mistiming of ECAL trigger inputs detailed in Section 5.1 is applied to the data-taking years 2016 and 2017.

The uncertainty in the integrated luminosity varies between 1.2–2.5% depending on the data-taking year, with an overall uncertainty of 1.6% for the 2016–2018 period [44–46].

The uncertainties considered in the analysis are presented in Table 5 with the pre-fit ranges corresponding to the maximum and minimum deviations of the event yields from their nominal values across each region, year of data-taking, category, recoil bin, and all SM background processes, when the respective systematic uncertainty is changed within ± 1 standard deviation. Most uncertainties are assumed uncorrelated from year to year when performing the fit. Those for which the source of the systematic uncertainty is identical for each year are treated as correlated. All systematic uncertainties are correlated across regions.

In addition to the uncertainties in Table 5, a photon normalisation uncertainty of 40% is included in the $\gamma +$ jets CR, to cover uncertainties in the translation between the $\gamma +$ jets and $\mathrm{Z} \to \ell\ell$ yields. The 100% normalisation uncertainty, also omitted from Table 5, is assigned to the predicted QCD multijet contribution to the SR, as described in Section 6.2.

The overall experimental uncertainty is found to be dominated by W tagging for the $\mathrm{t\bar{t}H}$ and b tagging for the VH categories in the SR. The lepton and photon candidate efficiencies for identification, isolation, and reconstruction, and uncertainties in the JER, JES, and trigger efficiencies also make significant contributions. The theoretical uncertainty is dominated by variations in the renormalisation scale, factorisation scale, and PDF for V + jets processes, although these are particularly sensitive to the high exclusive jet multiplicity characterising the $\mathrm{t\bar{t}H}$ and VH categories.

8 Results

The hadronic recoil distributions across all $\mathrm{t\bar{t}H}$ and VH subcategories are shown in Figs. 2 to 5. The predicted background yield from the fit to the CRs only is shown with the result of a fit including the data in the SR. Figure 2 (3) shows the $\mu +$ jets (e + jets) CR yields for the $\mathrm{t\bar{t}H}$ and VH categories, respectively, aggregated over 2016–2018. In these CRs, ℓ_{lost} background from $\mathrm{t\bar{t}}$, $\mathrm{W} \to \ell\nu$, and single t quark production dominates, with smaller contributions from multiboson and $\mathrm{t\bar{t}}$ processes. The $\mu\mu +$ jets, ee + jets, $\ell\ell +$ jets (only for $\mathrm{t\bar{t}H}$), and $\gamma +$ jets (only for VH) CR distributions used for the prediction of backgrounds stemming from $\mathrm{Z} \to$ inv decays are shown in Fig. 4 for 2016–2018. In addition, the total SM background prediction in the SR, consisting of ℓ_{lost}, $\mathrm{Z} \to$ inv, and QCD backgrounds, is shown for the $\mathrm{t\bar{t}H}$ and VH category in Fig. 5. The SR distributions contain all the Higgs boson production modes in the fitted $\mathcal{B}(\mathrm{H} \to \mathrm{inv})$ signal, including the ggH and VBF contamination in the $\mathrm{t\bar{t}H}$ and VH categories, with the prevalence of the ggH process due to its high production cross section. The post-fit event yields for each subcategory and recoil bin in the SR are tabulated in Table 6. For these results, a fit assuming $\mathcal{B}(\mathrm{H} \to \mathrm{inv}) = 0$ such that only SM background contributions are considered (B-only) is performed simultaneously using only the CRs (CR only), which are independent of the SR, or across both SR and CRs (CR+SR). A fit across all regions, including signal and background contributions (S+B fit), is also performed, in which the signal contribution is weighted by the best fit signal strength, $\mathcal{B}(\mathrm{H} \to \mathrm{inv})$. In all cases, uncertainties are inclusive of statistical and systematic contributions.

Table 5: The ranges corresponding to the maximum and minimum deviations of the event yields from their nominal values, provided where applicable across each region, year of data-taking, category, recoil bin, and all SM background processes, when the respective systematic uncertainty is changed within ± 1 standard deviation.

Systematic uncertainties on background yields (pre-fit)	Signal region		ℓ + jets		$\ell\ell$ + jets		γ + jets
	$t\bar{t}H$ cat.	VH cat.	$t\bar{t}H$ cat.	VH cat.	$t\bar{t}H$ cat.	VH cat.	VH cat.
Theoretical uncertainties							
Fact. scale V + jets (QCD)	<1.0-7.7 %	<1.0-19 %	<1.0-2.6 %	<1.0-11 %	<1.0-20 %	<1.0-22 %	6.0 %
Ren. scale V + jets (QCD)	<1.0-7.2 %	<1.0-8.6 %	<1.0-3.6 %	<1.0-10 %	<1.0-14 %	2.0-11 %	12 %
PDF V + jets	<1.0-9.1 %	2.0-23 %	<1.0-3.1 %	<1.0-15 %	<1.0-23 %	<1.0-26 %	8.0 %
Ren. & Fact. scale $t\bar{t}H$ (QCD)	<1.0-1.7 %	<1.0 %	<1.0-1.4 %	<1.0-1.4 %	<1.0 %	<1.0 %	—
Ren. & Fact. scale $t\bar{t}$ (QCD)	7.8-15 %	2.5-9.3 %	6.4-17 %	<1.0-6.3 %	<1.0-5.8 %	<1.0-5.8 %	—
NNLO QCD & NLO EW t quark p_T reweighting (inc. PDF)	<1.0-3.1 %	<1.0-1.2 %	<1.0-4.0 %	<1.0-3.9 %	<1.0 %	<1.0 %	—
Ren. & Fact. scale VV (QCD)	<1.0 %	<1.0 %	<1.0 %	<1.0 %	<1.0 %	<1.0 %	<1.0 %
$t\bar{t}H$ & VH cat. cross section (QCD)	5.8-9.2 %	<1.0-3.8 %	—	—	—	—	—
$t\bar{t}H$ & VH cat. cross section (PDF & α_s)	3.6 %	1.6-1.8 %	—	—	—	—	—
Initial-state radiation	2.0 %	3.0-6.0 %	2.0 %	<1.0-4.2 %	2.0 %	6.0 %	<1.0-4.0 %
Final-state radiation	5.0 %	3.0-5.0 %	2.0-2.2 %	<1.0-3.1 %	4.6-5.0 %	5.0 %	2.0-3.0 %
Experimental uncertainties							
Integrated luminosity	1.2-2.5 %	1.2-2.5 %	1.2-2.5 %	1.2-2.5 %	1.2-2.5 %	1.2-2.5 %	1.2-2.5 %
t-tagging	3.2-6.5 %	—	2.1-5.7 %	—	—	—	—
W-tagging	7.8-18 %	—	7.1-18 %	—	—	—	—
b-tagging	8.2-12 %	8.2-22 %	6.5-11 %	2.4-11 %	5.6-8.7 %	1.6-9.6 %	6.6-9.0 %
Electron identification & isolation	—	—	3.7-11 %	4.7-9.6 %	<1.0-15 %	<1.0-20 %	—
Electron reconstruction	—	—	<1.0-1.8 %	<1.0 %	1.0-1.5 %	<1.0-1.4 %	—
Muon identification	—	—	<1.0-1.0 %	<1.0-1.0 %	<1.0-1.8 %	<1.0-1.9 %	—
Muon isolation	—	—	<1.0 %	<1.0 %	<1.0 %	<1.0 %	—
Lepton veto	<1.0 %	<1.0 %	—	—	—	—	—
Photon identification & isolation	—	—	—	—	—	—	2.4-12 %
Photon reconstruction	—	—	—	—	—	—	<1.0 %
Pileup	1.4-8.8 %	<1.0-4.5 %	<1.0-4.8 %	<1.0-4.7 %	<1.0-2.1 %	<1.0-7.9 %	<1.0-3.3 %
Trigger inefficiency	<1.0-12 %	<1.0-1.4 %	<1.0-3.4 %	<1.0-2.4 %	<1.0-1.6 %	<1.0-1.5 %	<1.0-0.3 %
Trigger	2.0 %	2.0 %	2.0 %	2.0 %	2.0 %	2.0 %	2.0 %
Tau lepton veto	<1.0 %	<1.0 %	<1.0-1.0 %	<1.0-2.4 %	<1.0 %	<1.0 %	<1.0 %
JER	2.4-3.6 %	<1.0-1.1 %	1.7-3.0 %	<1.0-1.5 %	<1.0-3.5 %	<1.0-1.4 %	<1.0-2.9 %
JES	<1.0-6.3 %	<1.0-2.9 %	<1.0-5.0 %	<1.0-2.2 %	<1.0-6.7 %	<1.0-2.8 %	<1.0-3.8 %

The best fit value for $\hat{\mu}$ and corresponding 68 and 95% CL confidence intervals are extracted following the procedure outlined in Ref. [85] and Ref. [86]. The computing of upper limits adheres to the CLs criterion [87, 88] under the asymptotic approximation [81]. The upper limits on $\mathcal{B}(\mathrm{H} \to \mathrm{inv})$ as extracted from the likelihood fit presented in Section 7.1 are found to be 0.51 (0.53 expected) and 0.68 (0.53 expected) at 95% CL for the $t\bar{t}H$ and VH categories, respectively, with a combined upper limit of 0.47 (0.40 expected). These results are shown in Fig. 6 together with the observed and expected profile likelihood distribution. The expected distribution assumes $\mathcal{B}(\mathrm{H} \to \mathrm{inv}) = 0$. The results are compatible with the background expectation. The best fit $\mathcal{B}(\mathrm{H} \to \mathrm{inv})$ for the $t\bar{t}H$ and VH categories is $\hat{\mu} = 0.10^{+0.20}_{-0.18}(\mathrm{syst.})\ ^{+0.08}_{-0.08}(\mathrm{stat.})$ $(0.00^{+0.17}_{-0.17}(\mathrm{syst.})\ ^{+0.08}_{-0.08}(\mathrm{stat.}))$, where the pre-fit normalisation assumes $\mathcal{B}(\mathrm{H} \to \mathrm{inv}) = 1$. The systematic uncertainty with the largest impact on the $\mathcal{B}(\mathrm{H} \to \mathrm{inv})$ measurement for the $t\bar{t}H$ and VH categories using 2016–2018 data are those associated with the JES, while the statistical uncertainty contributes significantly to the overall uncertainty on $\mathcal{B}(\mathrm{H} \to \mathrm{inv})$. The breakdown of the impacts into uncertainty groups are presented in Table 7, together with the expectation assuming $\mathcal{B}(\mathrm{H} \to \mathrm{inv}) = 0$. The best fit estimate for the $t\bar{t}H$ (VH) category is $\hat{\mu} = -0.04^{+0.27}_{-0.27}$ $(0.00^{+0.26}_{-0.25})$ $(\hat{\mu} = 0.19^{+0.26}_{-0.27}$ $(0.00^{+0.27}_{-0.26}))$.

9 Combined H $\to$ inv limits

A variety of production modes of the Higgs boson can be used for searches for H $\to$ inv decays. A combination of the results of this analysis, analyses covering the years 2016–2018, and earlier published CMS combination results using Run 1 (years 2011–2012) and 2015 data [89] at $\sqrt{s} = 7$, 8, and 13 TeV, detailed in Table 8, is performed by means of a combined likelihood

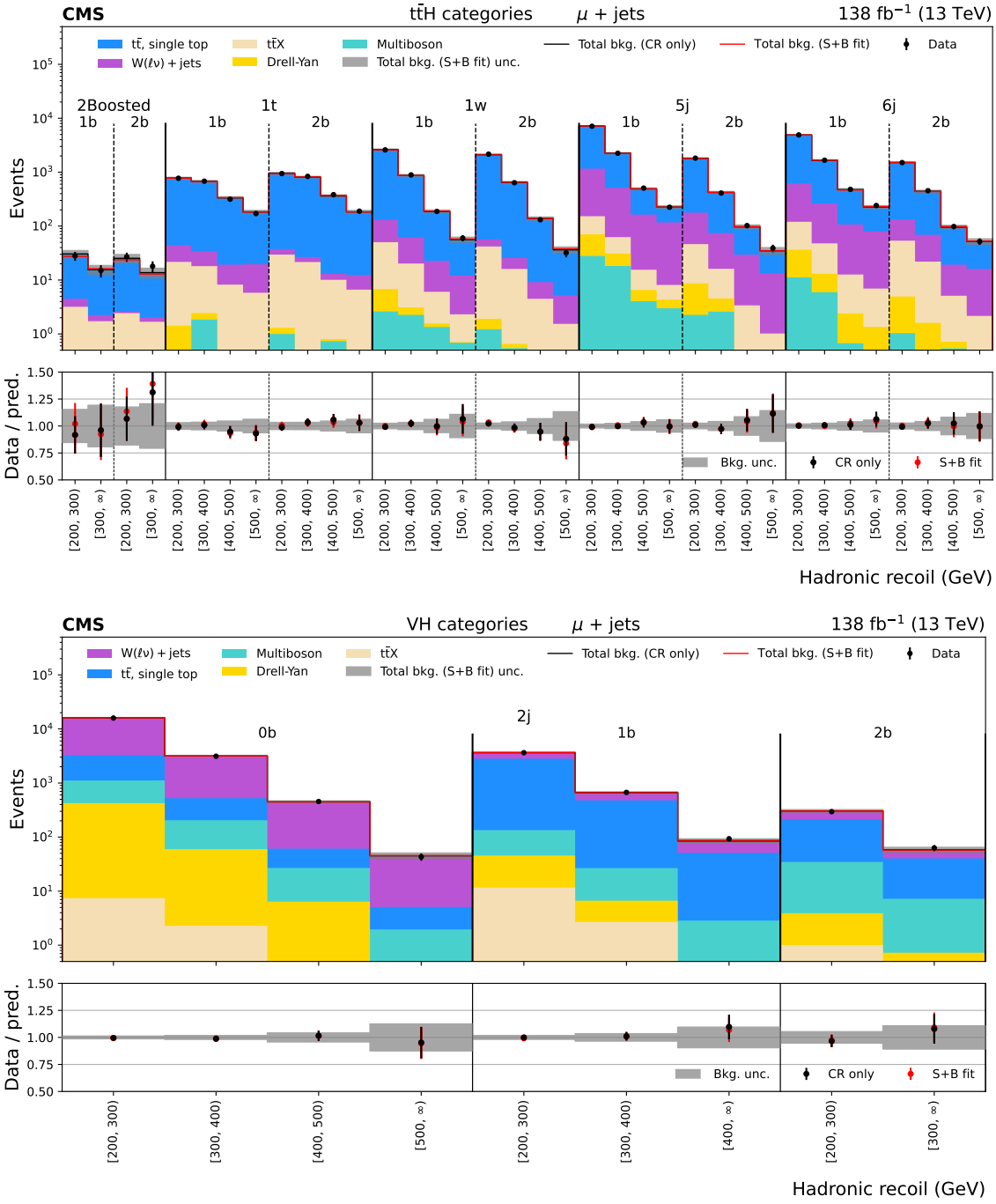

Figure 2: Distributions of hadronic recoil in the $t\bar{t}H$ (upper plot) and VH (lower plot) categories for the μ + jets CR. The black histogram shows the total background (bkg.) prediction from a CR only, B-only fit, while the red histogram shows the yields from a CR+SR S+B fit.

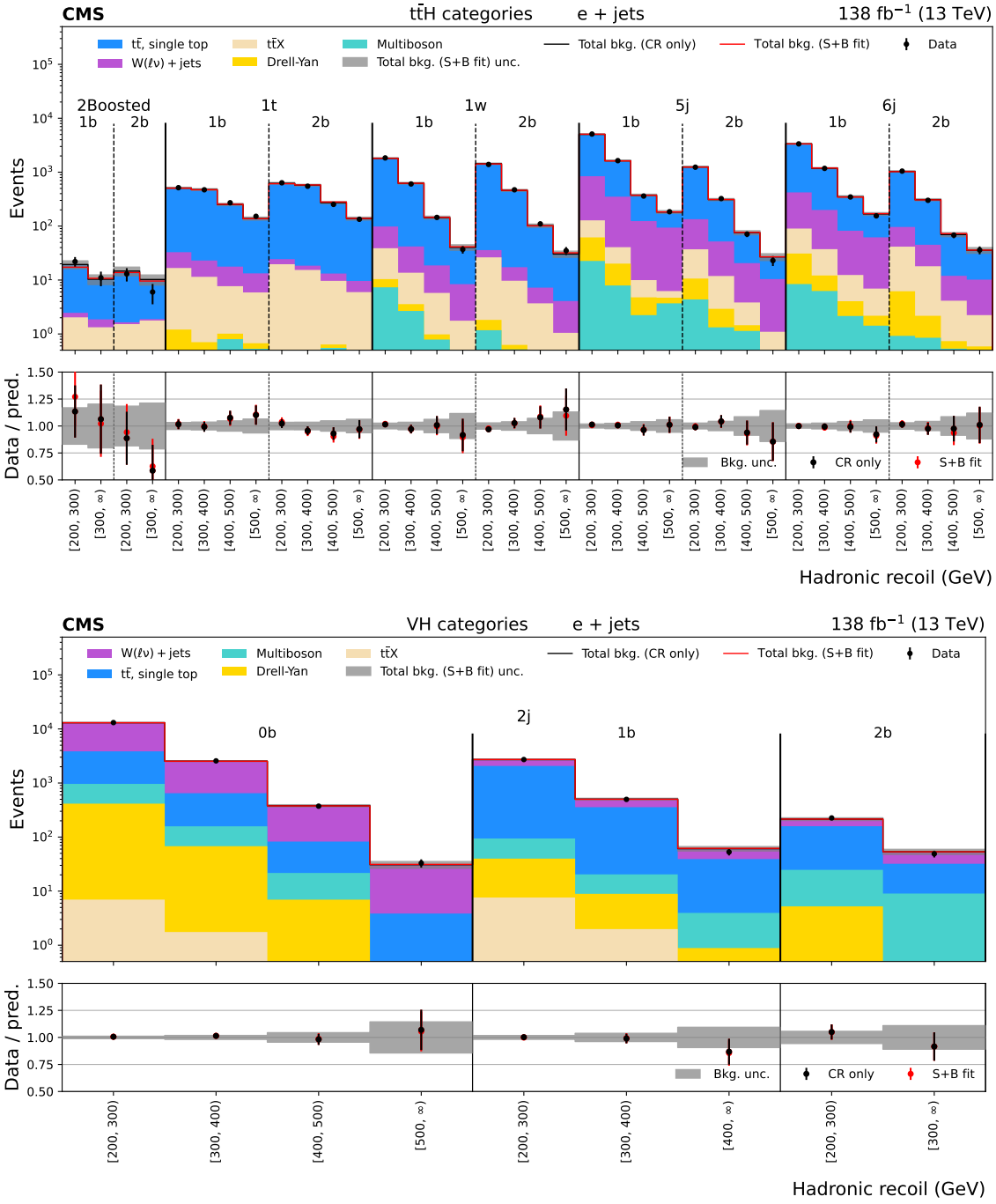

Figure 3: Distributions of hadronic recoil in the tt̄H (upper plot) and VH (lower plot) categories for the e + jets CR. The black histogram shows the total background (bkg.) prediction from a CR only, B-only fit, while the red histogram shows the yields from a CR+SR S+B fit.

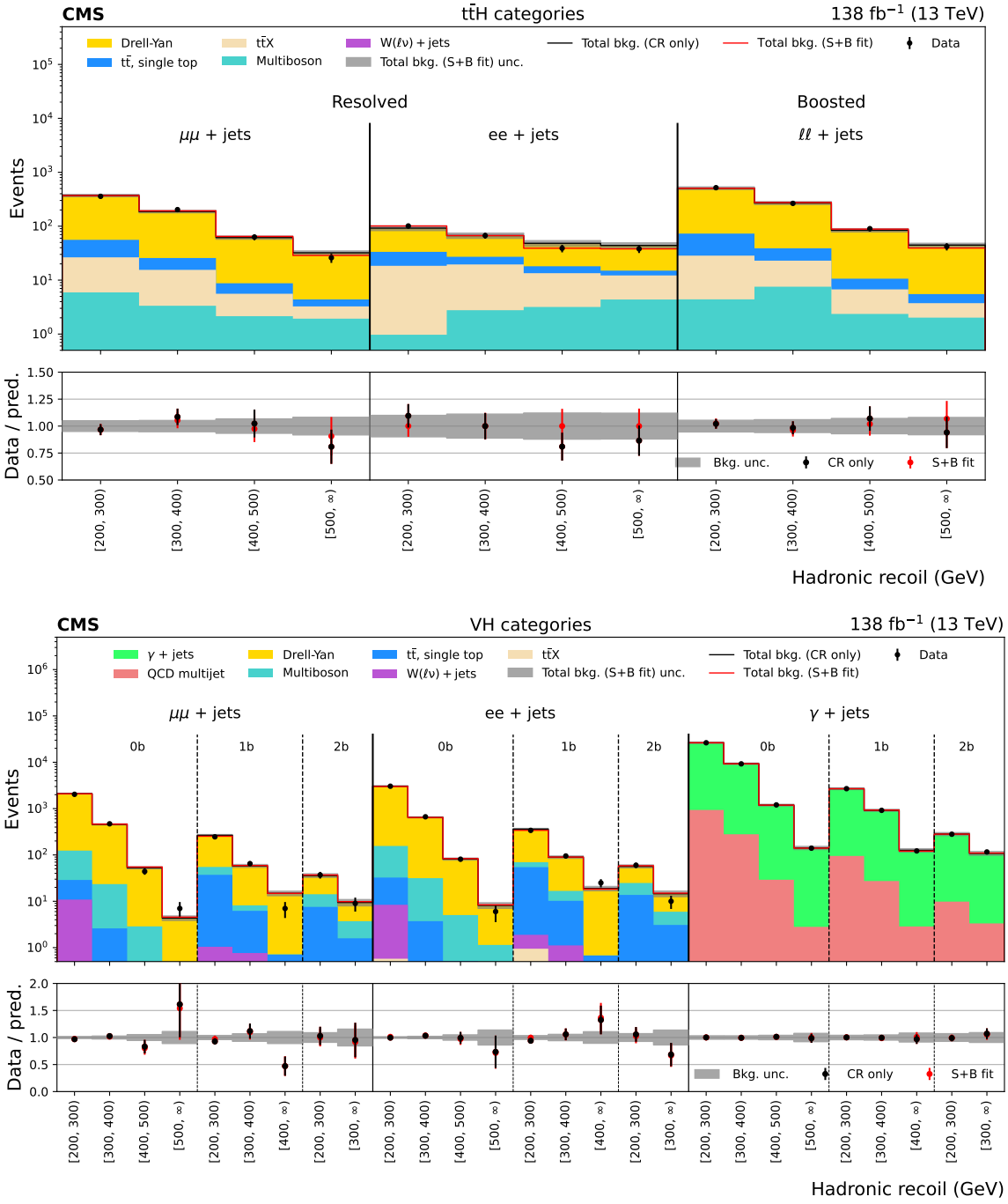

Figure 4: Distributions of hadronic recoil in the tt̄H category for the $\mu\mu$ + jets, ee + jets, and $\ell\ell$ + jets CRs (upper plot), and the VH category for the $\mu\mu$ + jets, ee + jets, and γ + jets CRs (lower plot). The black histogram shows the total background (bkg.) prediction from a CR only, B-only fit, while the red histogram shows the yields from a CR+SR S+B fit.

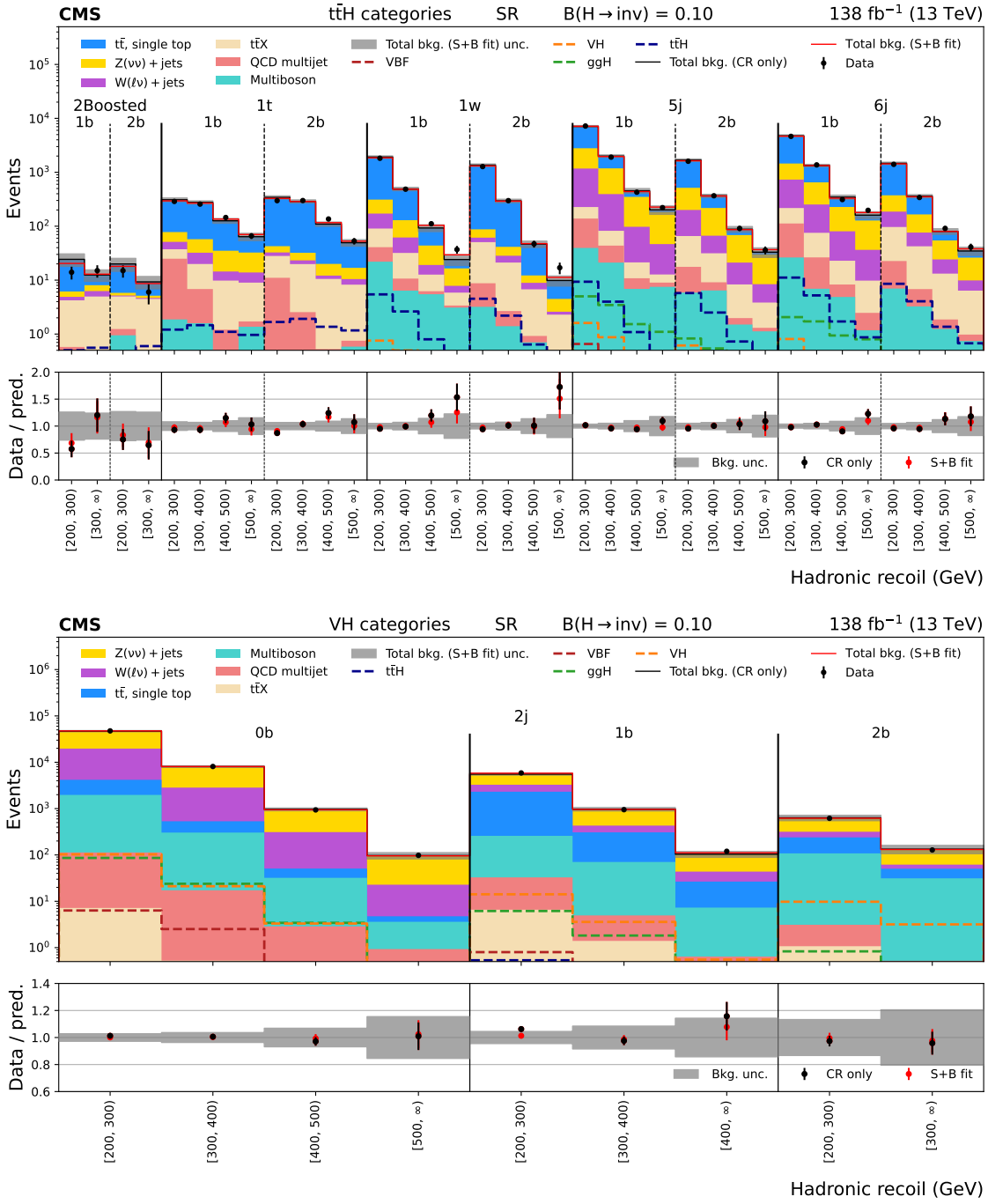

Figure 5: Distributions of hadronic recoil in the $t\bar{t}H$ (upper plot) and VH (lower plot) categories for the SR, showing the signal contributions from $t\bar{t}H$, VH, ggH, and VBF weighted by $\mathcal{B}(H \rightarrow \text{inv})$ =0.10. The black histogram shows the total background (bkg.) prediction from a CR only, B-only fit, while the red histogram shows the yields from a CR+SR S+B fit.

Table 6: Total post-fit yields in the SRs in each recoil bin and analysis category obtained by summing the contributions from the individual data-taking periods. B-only fits are performed for either CR+SR or CR only cases. The extracted signal yields from an S+B fit are also reported, where the signal strength is weighted by $\mathcal{B}(\mathrm{H} \to \mathrm{inv}) = 0.10$.

		ℓ_{lost}	$\mathrm{Z} \to \mathrm{inv}$	QCD	Total background			Signal
		CR only	CR only	CR only	CR only	CR + SR	Data	$\mathcal{B}(\mathrm{H} \to \mathrm{inv}) = 0.10$
Subcategory	Hadronic recoil	B-only fit	B-only fit	B-only fit	B-only fit	B-only fit		S+B fit
$t\bar{t}H$ 1t1b	[200, 300)	251.1 ± 9.5	35.2 ± 4.1	23.1 ± 16.8	309.4 ± 19.8	295.5 ± 11.6	288.0 ± 17.0	1.0 ± 0.8
	[300, 400)	235.2 ± 9.5	35.7 ± 5.0	5.2 ± 4.2	276.1 ± 11.5	268.1 ± 9.1	257.0 ± 16.0	1.3 ± 1.0
	[400, 500)	97.5 ± 5.3	27.6 ± 4.9	0.9 ± 0.6	126.1 ± 7.2	135.5 ± 6.7	145.0 ± 12.0	1.0 ± 0.8
	[500, ∞)	37.5 ± 2.9	26.1 ± 4.9	0.3 ± 0.3	63.9 ± 5.7	70.1 ± 5.1	66.0 ± 8.1	0.9 ± 0.7
$t\bar{t}H$ 1t2b	[200, 300)	312.5 ± 12.0	19.0 ± 2.2	10.9 ± 8.6	342.4 ± 14.9	328.1 ± 10.5	298.0 ± 17.3	1.4 ± 1.2
	[300, 400)	265.9 ± 10.7	20.2 ± 2.7	2.5 ± 1.7	288.6 ± 11.2	287.1 ± 9.3	299.0 ± 17.3	1.6 ± 1.3
	[400, 500)	93.6 ± 5.1	15.4 ± 2.6	0.4 ± 0.3	109.5 ± 5.7	116.5 ± 5.2	136.0 ± 11.7	1.2 ± 0.9
	[500, ∞)	35.4 ± 2.9	13.8 ± 2.5	$0.2 \pm <0.1$	49.4 ± 3.9	52.8 ± 3.5	53.0 ± 7.3	1.0 ± 0.8
$t\bar{t}H$ 1W1b	[200, 300)	1704.6 ± 49.9	190.7 ± 21.2	18.8 ± 16.8	1914.1 ± 56.8	1855.7 ± 41.2	1819.0 ± 42.6	5.7 ± 4.0
	[300, 400)	395.6 ± 15.1	90.2 ± 12.7	4.3 ± 2.9	490.0 ± 19.9	485.0 ± 16.2	486.0 ± 22.0	2.9 ± 1.9
	[400, 500)	56.2 ± 3.9	35.8 ± 6.5	0.8 ± 0.5	92.7 ± 7.7	103.7 ± 7.1	111.0 ± 10.5	0.9 ± 0.6
	[500, ∞)	9.9 ± 1.3	13.9 ± 2.9	$0.3 \pm <0.1$	24.1 ± 3.2	29.5 ± 3.0	37.0 ± 6.1	0.4 ± 0.3
$t\bar{t}H$ 1W2b	[200, 300)	1295.8 ± 40.7	53.1 ± 5.7	5.6 ± 3.8	1354.5 ± 41.3	1311.6 ± 29.4	1276.0 ± 35.7	3.9 ± 3.2
	[300, 400)	266.2 ± 11.8	27.2 ± 3.8	1.3 ± 0.9	294.7 ± 12.4	291.3 ± 9.9	298.0 ± 17.3	1.9 ± 1.6
	[400, 500)	38.3 ± 3.3	8.1 ± 1.5	$0.2 \pm <0.1$	46.6 ± 3.7	47.6 ± 3.1	47.0 ± 6.9	0.6 ± 0.4
	[500, ∞)	6.0 ± 1.0	3.7 ± 0.7	$0.1 \pm <0.1$	9.9 ± 1.2	11.3 ± 1.1	17.0 ± 4.1	$0.2 \pm <0.1$
$t\bar{t}H$ 2Boosted1b	[200, 300)	20.2 ± 3.6	3.8 ± 0.4	0.3 ± 0.3	24.3 ± 3.6	20.4 ± 2.6	14.0 ± 3.7	0.5 ± 0.3
	[300, ∞)	6.3 ± 1.4	6.1 ± 0.9	$0.1 \pm <0.1$	12.5 ± 1.7	12.9 ± 1.6	15.0 ± 3.9	0.5 ± 0.4
$t\bar{t}H$ 2Boosted2b	[200, 300)	15.8 ± 2.9	3.9 ± 0.9	$0.3 \pm <0.1$	20.0 ± 3.1	18.0 ± 2.4	15.0 ± 3.9	0.4 ± 0.3
	[300, ∞)	5.4 ± 1.3	3.8 ± 0.5	$0.1 \pm <0.1$	9.3 ± 1.4	8.6 ± 1.1	6.0 ± 2.4	0.5 ± 0.4
$t\bar{t}H$ 5j1b	[200, 300)	5279.7 ± 114.4	1703.7 ± 82.8	99.1 ± 78.5	7082.4 ± 161.6	7122.6 ± 127.6	7207.0 ± 84.9	14.4 ± 7.7
	[300, 400)	1135.0 ± 31.8	836.4 ± 50.0	22.5 ± 17.3	1994.0 ± 61.7	1960.9 ± 43.2	1907.0 ± 43.7	7.4 ± 3.8
	[400, 500)	182.2 ± 9.0	267.5 ± 24.9	4.0 ± 2.8	453.6 ± 26.6	438.8 ± 16.2	427.0 ± 20.7	2.7 ± 1.4
	[500, ∞)	54.2 ± 3.7	146.0 ± 20.3	1.5 ± 1.0	201.7 ± 20.6	226.2 ± 11.5	221.0 ± 14.9	1.5 ± 0.8
$t\bar{t}H$ 5j2b	[200, 300)	1317.8 ± 47.3	350.0 ± 16.6	11.8 ± 8.5	1679.6 ± 50.9	1635.4 ± 33.9	1602.0 ± 40.0	6.3 ± 4.2
	[300, 400)	188.7 ± 9.2	174.1 ± 10.4	2.7 ± 2.0	365.5 ± 14.1	363.3 ± 10.7	367.0 ± 19.2	2.9 ± 1.8
	[400, 500)	33.6 ± 3.5	53.8 ± 5.1	0.5 ± 0.3	87.9 ± 6.2	86.3 ± 4.5	91.0 ± 9.5	0.9 ± 0.5
	[500, ∞)	8.2 ± 1.4	24.6 ± 3.5	$0.2 \pm <0.1$	33.0 ± 3.8	36.8 ± 2.5	36.0 ± 6.0	0.5 ± 0.3
$t\bar{t}H$ 6j1b	[200, 300)	3851.5 ± 87.9	805.5 ± 38.8	85.9 ± 66.3	4742.9 ± 116.7	4672.6 ± 87.1	4632.0 ± 68.1	12.3 ± 8.1
	[300, 400)	876.0 ± 27.5	438.8 ± 26.1	19.5 ± 13.4	1334.2 ± 40.2	1332.5 ± 30.4	1371.0 ± 37.0	6.7 ± 4.0
	[400, 500)	179.6 ± 8.5	162.8 ± 15.4	3.4 ± 2.5	345.9 ± 17.8	330.9 ± 11.4	312.0 ± 17.7	2.4 ± 1.4
	[500, ∞)	61.0 ± 4.0	98.2 ± 13.6	1.3 ± 1.0	160.5 ± 14.3	179.1 ± 8.4	197.0 ± 14.0	1.6 ± 0.8
$t\bar{t}H$ 6j2b	[200, 300)	1214.0 ± 38.7	237.2 ± 11.4	15.6 ± 12.0	1466.8 ± 42.1	1433.1 ± 29.9	1404.0 ± 37.5	7.8 ± 6.1
	[300, 400)	237.9 ± 12.0	118.8 ± 7.1	3.6 ± 2.9	360.3 ± 14.2	351.9 ± 10.8	341.0 ± 18.5	3.8 ± 2.9
	[400, 500)	38.8 ± 3.8	40.9 ± 4.0	0.6 ± 0.4	80.3 ± 5.6	79.9 ± 4.3	91.0 ± 9.5	1.4 ± 1.0
	[500, ∞)	12.9 ± 1.7	21.6 ± 3.0	$0.2 \pm <0.1$	34.7 ± 3.5	38.1 ± 2.4	41.0 ± 6.4	0.7 ± 0.4
VH 2j0b	[200, 300)	17753.9 ± 373.6	29102.3 ± 655.5	105.8 ± 68.3	46962.1 ± 757.6	47499.1 ± 460.7	47559.0 ± 218.1	185.6 ± 92.5
	[300, 400)	2535.2 ± 69.4	5505.3 ± 155.0	16.8 ± 12.0	8057.3 ± 170.3	8075.7 ± 106.8	8106.0 ± 90.0	44.3 ± 23.0
	[400, 500)	278.9 ± 16.1	684.1 ± 34.7	2.8 ± 1.8	965.8 ± 38.3	944.5 ± 26.7	938.0 ± 30.6	6.6 ± 3.4
	[500, ∞)	19.2 ± 3.1	76.9 ± 8.1	0.9 ± 0.5	97.1 ± 8.7	95.7 ± 6.6	98.0 ± 9.9	0.6 ± 0.3
VH 2j1b	[200, 300)	3020.1 ± 84.0	2490.4 ± 114.7	26.2 ± 24.5	5536.8 ± 144.3	5808.6 ± 111.1	5883.0 ± 76.7	20.3 ± 10.0
	[300, 400)	360.1 ± 17.3	609.0 ± 44.1	3.6 ± 3.0	972.7 ± 47.5	962.3 ± 30.1	949.0 ± 30.8	5.2 ± 2.8
	[400, ∞)	36.3 ± 4.5	66.7 ± 7.3	0.6 ± 0.5	103.7 ± 8.6	111.3 ± 7.7	120.0 ± 11.0	0.7 ± 0.4
VH 2j2b	[200, 300)	209.4 ± 14.0	422.3 ± 46.6	2.0 ± 1.2	633.7 ± 48.6	620.1 ± 26.8	617.0 ± 24.8	10.8 ± 7.9
	[300, ∞)	30.7 ± 3.5	102.6 ± 15.4	$0.2 \pm <0.1$	133.6 ± 15.8	131.1 ± 9.8	128.0 ± 11.3	3.5 ± 2.5

Table 7: The observed and expected impacts on $\mathcal{B}(\mathrm{H} \to \mathrm{inv})$ for different groups of uncertainties, where the expected results are produced with $\mathcal{B}(\mathrm{H} \to \mathrm{inv}) = 0$.

Uncertainty group	Impact on $\mathcal{B}(\mathrm{H} \to \mathrm{inv})$	
	Observed	Expected
Jet calibration	$^{+0.12}_{-0.11}$	$^{+0.11}_{-0.10}$
Lepton veto	± 0.05	± 0.05
Lepton/photon identification	$^{+0.07}_{-0.06}$	$^{+0.06}_{-0.05}$
Theory	$^{+0.06}_{-0.05}$	$^{+0.04}_{-0.03}$
Integrated luminosity/pileup	± 0.03	± 0.03
QCD prediction	± 0.02	± 0.02
Boosted object/b jet tagging	± 0.02	± 0.02
Triggers	± 0.04	± 0.03
Stat. uncertainty of simulation	± 0.08	± 0.08
Other uncertainties	± 0.10	± 0.10

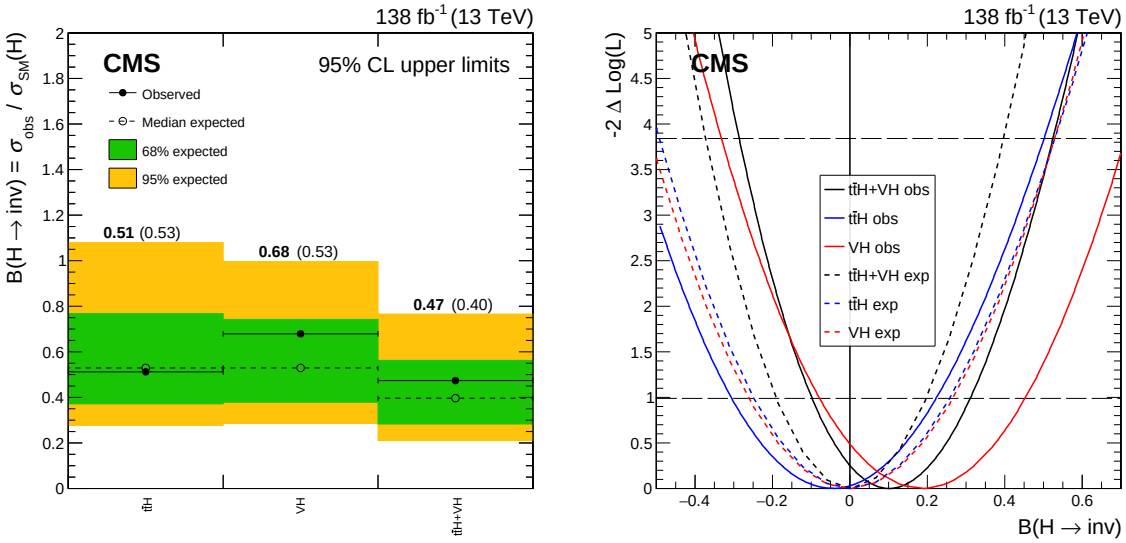

Figure 6: Left: Observed and expected limits at 95% CL for the $t\bar{t}H$ and VH categories using 2016–2018 data. Right: The profile likelihood scan corresponding to observed and expected (where $\mathcal{B}(H \to \text{inv}) = 0$) limits in the fit to the $t\bar{t}H$ and VH categories.

fit in which systematic uncertainties are correlated across search regions where appropriate. Unless explicitly specified below, parameters of the individual likelihood functions are treated as independent.

Table 8: Data sets and their respective integrated luminosities used for each production mode across Run 1 and Run 2. For some data-taking periods, no $H \to$ inv search have been performed for the given production mode, and are not included in the combination.

Analysis tag	Production mode	Integrated luminosity (fb^{-1})		
		7 TeV	8 TeV	13 TeV (Run 2)
VBF-tagged	VBF	—	19.2 [90]	140 [89][34]
VH-tagged	$Z(\ell\ell)H$	4.9 [90]	19.7 [90]	140 [89][32]
	$Z(b\bar{b})H$	—	18.9 [90]	—
	$V(jj)H$	—	19.7 [91]	140 [89][this paper]
	Boosted VH	—	—	138 [33]
$t\bar{t}H$-tagged	$t\bar{t}H$ (hadronic)	—	—	138 [this paper]
	$t\bar{t}H$ (leptonic)	—	—	138 [29, 30]
ggH-tagged	ggH	—	19.7 [91]	140 [89][33]

For the $t\bar{t}H$ analysis with fully leptonic final states, a reinterpretation of the supersymmetry searches in the semileptonic and dileptonic $t\bar{t}$ decay channels in Ref. [29, 30] in the context of the $t\bar{t}$ + DM model studied in Ref. [31] has been performed. Another leptonic channel included in this combination is from the $Z(\ell\ell)H$ analysis [32] using 2016–2018 data.

Analyses with hadronic final states partially overlap in their phase space selection, and this must be accounted for in the statistical combination. Those affected by overlap are the VBF analysis [34], the analysis targetting hadronic ggH and boosted VH final states [33], and the resolved VH channel described in this paper.

To remove the overlap between the VBF analysis and ggH/boosted VH analysis, events are considered for rejection in the ggH/boosted VH analysis if they have at least two AK4 jets each

with $|\eta| < 4.7$. Specifically, an inversion of the VBF kinematic selection is applied similarly to the $t\bar{t}H$ and resolved VH analysis as described in Section 5.2. These requirements mirror the selection used to enhance the characteristic VBF phase space in Ref. [34], with negligible effect on the sensitivity of the ggH/boosted VH analysis to $\mathcal{B}(H \to \text{inv})$.

The overlap between the ggH/boosted VH analysis and the VH 2j0b category of this analysis is driven by the low-purity VH category of the boosted analysis. By removing events from the low-purity boosted VH category that contain exactly two AK4 jets forming a dijet candidate with $65 < m_{jj} < 120\,\text{GeV}$, there is negligible reduction in the exclusion sensitivity of that analysis. The overlap meanwhile is reduced from 30-40% in the CR phase spaces to about 1%.

The uncertainties in the overall cross section for the signal processes are treated as correlated amongst analysis channels, and amongst data sets with the same centre-of-mass energy. The uncertainties related to missing higher-order corrections, as well as PDF variations, are obtained from Ref. [58]. In some of the channels, additional uncertainty contributions relating to signal acceptance modelling are considered. These are treated as uncorrelated amongst the different analysis channels.

The main sources of theoretical modelling uncertainties in the background estimate vary for the different analysis channels. The analyses preferentially select different phase space regions, and employ different assumptions for the modelling of theoretical uncertainties in transfer factors amongst different analysis regions. The resulting uncertainties are therefore treated as uncorrelated.

Significant correlations appear in the treatment of experimental uncertainties. The determination of the integrated luminosity estimate is affected by a number of sources of uncertainty, which are assumed to be correlated amongst all channels, and partially correlated amongst data sets. Some of the analysis channels share trigger requirements, and the uncertainties in the efficiencies of these common triggers are assumed to be correlated amongst channels and uncorrelated amongst data sets. Furthermore, analysis channels often share criteria used for identifying b-tagged jets, as well as the hadronic decay products of tau leptons. The uncertainties in the efficiencies of these identification criteria are assumed to be correlated amongst channels using the same criteria in the same data set. Finally, uncertainties in the calibration of the JER and JES are treated as correlated amongst this analysis, the VBF, and the ggH/boosted VH channels. All other experimental uncertainties are assumed to be uncorrelated amongst channels. For earlier analyses using Run 1 and 2015 data, the correlation scheme established in Ref. [89] is used.

Exclusion limits on $\mathcal{B}(H \to \text{inv})$ are calculated assuming SM production cross sections. The 2016–2018 data yields an overall limit of 0.16 (0.09 expected). If the Run 1 and 2015 data-taking periods are included, values larger than 0.15 (0.08 expected) are excluded at 95% CL. This value is dominated by the VBF channel, which yields a limit for $\mathcal{B}(H \to \text{inv})$ of 0.18 (0.10 expected). The limits for Run 1 and Run 2, separated by the Higgs boson production mode as tagged by the input analyses, are presented in Fig. 7. The integrated luminosities of the Run 1 and Run 2 data sets [31–34, 89] are described in Table 8. The final combination represents an improvement in sensitivity of approximately 20% relative to the most sensitive single channel (VBF).

Maximum likelihood fits to the individual production channels are performed, as well as to the combination of all channels. The dependence of the profile negative log-likelihood functions on the signal strength parameter $\hat{\mu}$ is shown in Fig. 7 (right). The best fit values of $\hat{\mu}$ for the individual production channels are compatible with one another and with the combined value of $0.08^{+0.04}_{-0.04}$, and the observed signal strength is compatible with the absence of a $H \to \text{inv}$ signal

within two standard deviations. A breakdown of the best fit values of $\hat{\mu}$ for each channel are presented in Table 9. A saturated goodness-of-fit test is performed using the final combined likelihood function [92], yielding a probability of 12% that the S+B model is consistent with the observed results from the CMS experiment. Tabulated yields and fit results are provided in HEPData [93].

Table 9: The observed best fit estimates of $\mathcal{B}(\mathrm{H} \to \mathrm{inv})$, for each analysis channel in the combination, and the 95% CL observed and expected (exp) upper limits on $\mathcal{B}(\mathrm{H} \to \mathrm{inv})$.

Channel	Best fit $\mathcal{B}(\mathrm{H} \to \mathrm{inv})$	$\mathcal{B}(\mathrm{H} \to \mathrm{inv})$
Combined	$0.08^{+0.04}_{-0.04}$	0.15 (0.08 exp)
VBF-tag	$0.09^{+0.05}_{-0.05}$	0.18 (0.10 exp)
VH-tag	$0.04^{+0.09}_{-0.09}$	0.21 (0.18 exp)
$\mathrm{t\bar{t}H}$-tag	$-0.08^{+0.16}_{-0.16}$	0.26 (0.30 exp)
ggH-tag	$0.22^{+0.16}_{-0.16}$	0.49 (0.32 exp)

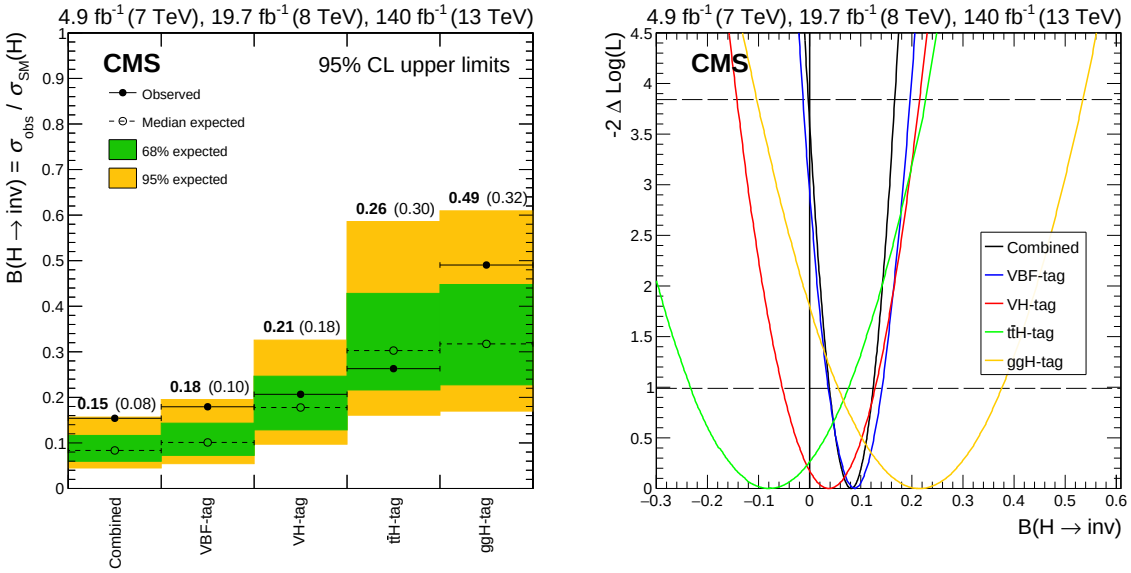

Figure 7: Left: Exclusion limits at 95% CL on $\mathcal{B}(\mathrm{H} \to \mathrm{inv})$. The results are shown separately for each Higgs boson production mode as tagged by the input analyses for Run 1 and Run 2, as well as combined across modes. Right: Scan of the profile negative log-likelihood as a function of $\mathcal{B}(\mathrm{H} \to \mathrm{inv})$ broken down by the Higgs boson production mode as tagged by the input analyses for Run 1 and Run 2.

The upper limit on $\mathcal{B}(\mathrm{H} \to \mathrm{inv})$ is interpreted in the context of a set of Higgs portal models of DM interactions, where a stable weakly interacting massive particle (WIMP), such as a singlet scalar, fermion, or vector, has a substantial coupling to a Higgs boson of mass 125 GeV [19, 20]. The interaction of a WIMP with an atomic nucleus can occur via the exchange of a Higgs boson, and the resulting nuclear recoil is measured to obtain an upper bound on the spin-independent DM-nucleon scattering cross section, $\sigma^{\mathrm{SI}}_{\text{DM-nucleon}}$. An effective field theory (EFT) approach is considered for scalar and fermionic WIMPs, while in the vectorial case two UV-complete DM models are considered, given the EFT appraoch violates unitarity [23, 94]. The vector-spin WIMP model (Vector $\mathrm{DM}^{\text{UV-comp}}$) described in Ref. [20], and its radiative portal analogue (Vector $\mathrm{DM}^{\text{radiative}}_{m_2}$) introduced in Ref. [23] for dark Higgs boson masses $m_2 = 65$ and 100 GeV, and with a mixing angle between the SM and dark Higgs bosons $\theta = 0.2$, are presented. The results are compared to direct-detection searches, where in these experiments

it is assumed DM particles interact with atomic nuclei. Direct-detection limits are reported by the CRESST-III [95], DarkSide-50 [96], Panda-X 4T [97], and LUX-ZEPLIN [98] experiments. For the CRESST-III limits, a range of masses from $m_{\mathrm{DM}} = 150\,\mathrm{MeV}$ and above are reported, however for this paper only values above $m_{\mathrm{DM}} = 1\,\mathrm{GeV}$ are used. Upper limits on $\sigma^{\mathrm{SI}}_{\mathrm{DM\text{-}nucleon}}$ for a range of DM mass points are presented in Fig. 8 at the 90% CL using the full CMS data set. The uncertainties in $\sigma^{\mathrm{SI}}_{\mathrm{DM\text{-}nucleon}}$ are obtained from the extrema of a coupling parametrisation factor as derived from lattice theory [19, 99, 100]. Results of the Higgs portal interpretation and direct-detection comparison are also provided in HEPData [93].

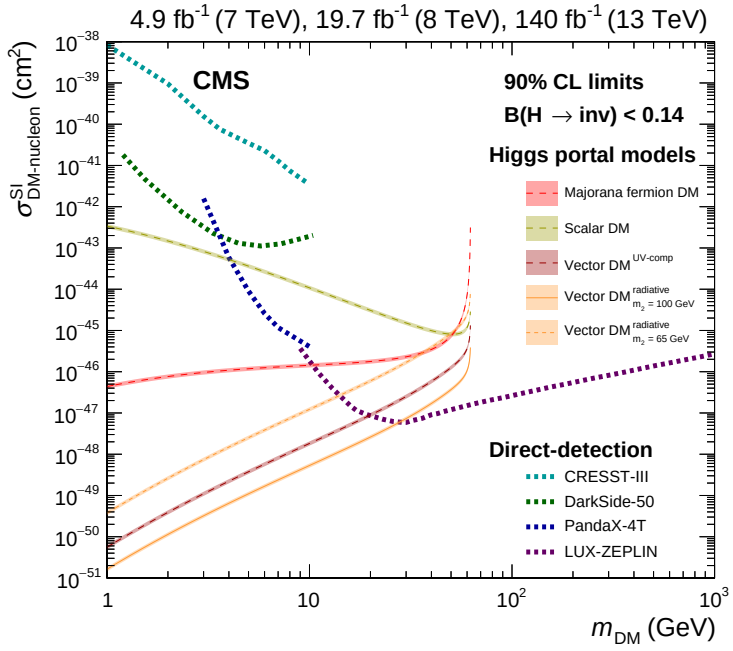

Figure 8: Upper limits on $\sigma^{\mathrm{SI}}_{\mathrm{DM\text{-}nucleon}}$ as a function of DM candidate mass m_{DM}. Results are presented for a fermion (red) and scalar (yellow) DM candidate. In addition, a vector DM candidate is studied using two UV-comp approaches, the first denoted Vector DM$^{\mathrm{UV\text{-}comp}}$ [20] (burgundy), and the second a radiative portal version denoted Vector DM$^{\mathrm{radiative}}_{m_2}$ [23] (orange) with a dark Higgs boson mass of $m_2 = 65$ and 100 GeV. Uncertainties are derived from Refs. [19, 99, 100]. Results are compared to direct-detection searches from CRESST-III [95] (truncated at $m_{\mathrm{DM}} > 1\,\mathrm{GeV}$), DarkSide-50 [96], PandaX-4T [97] and LUX-ZEPLIN [98].

The sensitivity of the Run 1 and Run 2 combination depends on the cross sections assumed for the different Higgs boson production modes: VBF, VH, ggH, and $\mathrm{t\bar{t}H}$. Cross sections can be parameterised by the coupling strength of the Higgs boson to V bosons and fermions. The cross sections can be directly scaled by coupling strength modifiers κ_{V} and κ_{F} to investigate BSM scenarios [101]. In this context, the observed 95% CL upper limits on $\mathcal{B}(\mathrm{H} \to \mathrm{inv})$ are evaluated as a function of κ_{V} and κ_{F} and shown in Fig. 9. Best estimates of κ_{V} and κ_{F} from CMS [11] are presented with the 68 and 95% CL contours. For the best estimate of κ_{V} and κ_{F} by CMS, the 95% CL limit on $\mathcal{B}(\mathrm{H} \to \mathrm{inv})$ is found to be 0.16, and varies between 0.14 and 0.17 inside the 95% CL contour.

10 Summary

The results of a search for invisible decays of the Higgs boson produced in association with a top-antitop quark pair ($\mathrm{t\bar{t}H}$) or a vector boson (VH, where V stands for either a W or Z

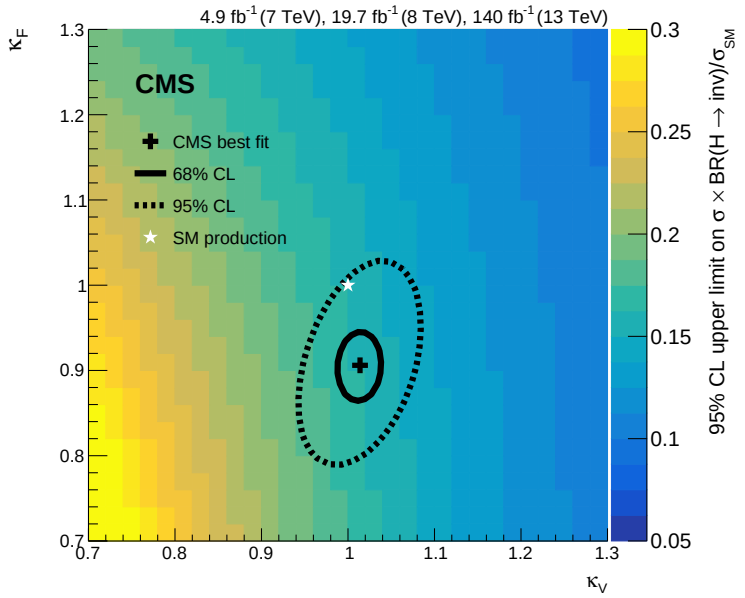

Figure 9: Observed 95% CL upper limit on $\mathcal{B}(\mathrm{H} \to \mathrm{inv})$ as a function of coupling strength modifiers, κ_V and κ_F, for a Higgs boson of mass 125 GeV. Best estimates for κ_V and κ_F from Ref. [11] are shown as a black cross, together with 68 and 95% CL contours.

boson), which decays to a fully hadronic final state, are presented. The analysis is based on proton-proton collision data collected at $\sqrt{s} = 13$ TeV during the 2016–2018 data-taking period by the CMS experiment at the LHC, corresponding to an integrated luminosity of 138 fb^{-1}. The $\mathrm{t\bar{t}H}$ production mechanism is investigated using final states containing b jets, or boosted t quarks or W bosons. The VH production channel focuses on resolving a dijet pair with an invariant mass that is compatible with that of a W or Z boson. No significant excess of events is observed above the predicted SM background. A 95% confidence level upper limit of 0.47 (0.40 expected) is set on the branching fraction of the decay of the Higgs boson to an invisible final state, $\mathcal{B}(\mathrm{H} \to \mathrm{inv})$, assuming SM production cross sections.

The results are combined with previous $\mathcal{B}(\mathrm{H} \to \mathrm{inv})$ searches carried out at $\sqrt{s} = 7$, 8, and 13 TeV in complementary production modes. The combined 95% confidence level upper limit on $\mathcal{B}(\mathrm{H} \to \mathrm{inv})$ of 0.15 (0.08 expected) is obtained using Run 1 (2011–2012) and Run 2 (2015–2018) data. The combination represents an improvement in sensitivity of 20% relative to the most sensitive single channel. The results are interpreted in the context of a set of Higgs portal models of dark matter interactions to produce model-dependent exclusion limits that complement direct-detection experiments for light mass dark matter candidates.

References

[1] F. Englert and R. Brout, "Broken symmetry and the mass of gauge vector mesons", *Phys. Rev. Lett.* **13** (1964) 321, doi:10.1103/PhysRevLett.13.321.

[2] P. W. Higgs, "Broken symmetries, massless particles and gauge fields", *Phys. Lett.* **12** (1964) 132, doi:10.1016/0031-9163(64)91136-9.

[3] P. W. Higgs, "Broken symmetries and the masses of gauge bosons", *Phys. Rev. Lett.* **13** (1964) 508, doi:10.1103/PhysRevLett.13.508.

[4] G. S. Guralnik, C. R. Hagen, and T. W. B. Kibble, "Global conservation laws and massless particles", *Phys. Rev. Lett.* **13** (1964) 585, doi:10.1103/PhysRevLett.13.585.

[5] P. W. Higgs, "Spontaneous symmetry breakdown without massless bosons", *Phys. Rev.* **145** (1966) 1156, doi:10.1103/PhysRev.145.1156.

[6] T. W. B. Kibble, "Symmetry breaking in non-abelian gauge theories", *Phys. Rev.* **155** (1967) 1554, doi:10.1103/PhysRev.155.1554.

[7] ATLAS Collaboration, "Observation of a new particle in the search for the standard model Higgs boson with the ATLAS detector at the LHC", *Phys. Lett. B* **716** (2012) 1, doi:10.1016/j.physletb.2012.08.020, arXiv:1207.7214.

[8] CMS Collaboration, "Observation of a new boson at a mass of 125 GeV with the CMS experiment at the LHC", *Phys. Lett. B* **716** (2012) 30, doi:10.1016/j.physletb.2012.08.021, arXiv:1207.7235.

[9] CMS Collaboration, "Observation of a new boson with mass near 125 GeV in pp collisions at $\sqrt{s}$ = 7 and 8 TeV", *JHEP* **06** (2013) 081, doi:10.1007/JHEP06(2013)081, arXiv:1303.4571.

[10] ATLAS Collaboration, "A detailed map of Higgs boson interactions by the ATLAS experiment ten years after the discovery", *Nature* **607** (2022) 52, doi:10.1038/s41586-022-04893-w, arXiv:2207.00092.

[11] CMS Collaboration, "A portrait of the Higgs boson by the CMS experiment ten years after the discovery", *Nature* **607** (2022) 60, doi:10.1038/s41586-022-04892-x, arXiv:2207.00043.

[12] Particle Data Group, "Review of particle physics", *PTEP* **2022** (2022) 083C01, doi:10.1093/ptep/ptac097.

[13] R. E. Shrock and M. Suzuki, "Invisible decays of Higgs bosons", *Phys. Lett. B* **110** (1982) 250, doi:10.1016/0370-2693(82)91247-3.

[14] G. Bélanger et al., "The MSSM invisible Higgs in the light of dark matter and g-2", *Phys. Lett. B* **519** (2001) 93, doi:10.1016/S0370-2693(01)00976-5, arXiv:hep-ph/0106275.

[15] A. Datta, K. Huitu, J. Laamanen, and B. Mukhopadhyaya, "Linear collider signals of an invisible Higgs boson in theories of large extra dimensions", *Phys. Rev. D* **70** (2004) 075003, doi:10.1103/PhysRevD.70.075003, arXiv:hep-ph/0404056.

[16] D. Dominici and J. F. Gunion, "Invisible Higgs decays from Higgs-graviscalar mixing", *Phys. Rev. D* **80** (2009) 115006, doi:10.1103/PhysRevD.80.115006, arXiv:0902.1512.

[17] S. Argyropoulos, O. Brandt, and U. Haisch, "Collider searches for dark matter through the Higgs lens", *Symmetry* **13** (2021), no. 12, 2406, doi:10.3390/sym13122406, arXiv:2109.13597.

[18] S. Kanemura, S. Matsumoto, T. Nabeshima, and N. Okada, "Can WIMP dark matter overcome the nightmare scenario?", *Phys. Rev. D* **82** (2010) 055026, doi:10.1103/PhysRevD.82.055026, arXiv:1005.5651.

[19] A. Djouadi, O. Lebedev, Y. Mambrini, and J. Quevillon, "Implications of LHC searches for Higgs–portal dark matter", *Phys. Lett. B* **709** (2012) 65, doi:10.1016/j.physletb.2012.01.062, arXiv:1112.3299.

[20] S. Baek, P. Ko, W.-I. Park, and E. Senaha, "Higgs portal vector dark matter: revisited", *JHEP* **05** (2013) 036, doi:10.1007/JHEP05(2013)036, arXiv:1212.2131.

[21] A. Djouadi, A. Falkowski, Y. Mambrini, and J. Quevillon, "Direct detection of Higgs–portal dark matter at the LHC", *Eur. Phys. J. C* **73** (2013) 2455, doi:10.1140/epjc/s10052-013-2455-1, arXiv:1205.3169.

[22] A. Beniwal et al., "Combined analysis of effective Higgs–portal dark matter models", *Phys. Rev. D* **93** (2016) 115016, doi:10.1103/PhysRevD.93.115016, arXiv:1512.06458.

[23] A. DiFranzo, P. J. Fox, and T. M. P. Tait, "Vector dark matter through a radiative Higgs portal", *JHEP* **04** (2016) 135, doi:10.1007/JHEP04(2016)135, arXiv:1512.06853.

[24] ATLAS Collaboration, "Search for an invisibly decaying Higgs boson or dark matter candidates produced in association with a Z boson in pp collisions at $\sqrt{s}$ = 13 TeV with the ATLAS detector", *Phys. Lett. B* **776** (2018) 318, doi:10.1016/j.physletb.2017.11.049, arXiv:1708.09624.

[25] ATLAS Collaboration, "Combination of searches for invisible Higgs boson decays with the ATLAS experiment", *Phys. Rev. Lett.* **122** (2019) 231801, doi:10.1103/PhysRevLett.122.231801, arXiv:1904.05105.

[26] ATLAS Collaboration, "Search for new phenomena in events with an energetic jet and missing transverse momentum in pp collisions at $\sqrt{s}$ = 13 TeV with the ATLAS detector", *Phys. Rev. D* **103** (2021) 112006, doi:10.1103/PhysRevD.103.112006, arXiv:2102.10874.

[27] ATLAS Collaboration, "Search for associated production of a z boson with an invisibly decaying Higgs boson or dark matter candidates at $\sqrt{s}$ = 13 TeV with the ATLAS detector", *Phys. Lett. B* **829** (2022) 137066, doi:10.1016/j.physletb.2022.137066, arXiv:2111.08372.

[28] ATLAS Collaboration, "Search for invisible Higgs-boson decays in events with vector-boson fusion signatures using 139 fb^{-1} of proton-proton data recorded by the ATLAS experiment", *JHEP* **08** (2022) 104, doi:10.1007/JHEP08(2022)104, arXiv:2202.07953.

[29] CMS Collaboration, "Search for direct top squark pair production in events with one lepton, jets, and missing transverse momentum at 13 TeV with the CMS experiment", *JHEP* **05** (2020) 032, doi:10.1007/JHEP05(2020)032, arXiv:1912.08887.

[30] CMS Collaboration, "Search for top squark pair production using dilepton final states in pp collision data collected at $\sqrt{s}$ = 13 TeV", *Eur. Phys. J. C* **81** (2021) 3, doi:10.1140/epjc/s10052-020-08701-5, arXiv:2008.05936.

[31] CMS Collaboration, "Combined searches for the production of supersymmetric top quark partners in proton-proton collisions at $\sqrt{s}$ = 13 TeV", *Eur. Phys. J. C* **81** (2021) 970, doi:10.1140/epjc/s10052-021-09721-5, arXiv:2107.10892.

[32] CMS Collaboration, "Search for dark matter produced in association with a leptonically decaying z boson in proton-proton collisions at $\sqrt{s} = 13$ TeV", *Eur. Phys. J. C* **81** (2021) 13, doi:10.1140/epjc/s10052-020-08739-5, arXiv:2008.04735. [Erratum: doi:10.1140/epjc/s10052-021-08959-3].

[33] CMS Collaboration, "Search for new particles in events with energetic jets and large missing transverse momentum in proton-proton collisions at $\sqrt{s} = 13$ TeV", *JHEP* **11** (2021) 153, doi:10.1007/JHEP11(2021)153, arXiv:2107.13021.

[34] CMS Collaboration, "Search for invisible decays of the Higgs boson produced via vector boson fusion in proton-proton collisions at $\sqrt{s} = 13$ TeV", *Phys. Rev. D* **105** (2022) 092007, doi:10.1103/PhysRevD.105.092007, arXiv:2201.11585.

[35] CMS Collaboration, "Performance of the CMS level-1 trigger in proton-proton collisions at $\sqrt{s} = 13$ TeV", *JINST* **15** (2020) P10017, doi:10.1088/1748-0221/15/10/P10017, arXiv:2006.10165.

[36] CMS Collaboration, "The CMS trigger system", *JINST* **12** (2017) P01020, doi:10.1088/1748-0221/12/01/P01020, arXiv:1609.02366.

[37] CMS Collaboration, "Electron and photon reconstruction and identification with the CMS experiment at the CERN LHC", *JINST* **16** (2021) P05014, doi:10.1088/1748-0221/16/05/P05014, arXiv:2012.06888.

[38] CMS Collaboration, "Performance of the CMS muon detector and muon reconstruction with proton-proton collisions at $\sqrt{s} = 13$ TeV", *JINST* **13** (2018) P06015, doi:10.1088/1748-0221/13/06/P06015, arXiv:1804.04528.

[39] CMS Collaboration, "Description and performance of track and primary-vertex reconstruction with the CMS tracker", *JINST* **9** (2014) P10009, doi:10.1088/1748-0221/9/10/P10009, arXiv:1405.6569.

[40] CMS Collaboration, "Particle-flow reconstruction and global event description with the CMS detector", *JINST* **12** (2017) P10003, doi:10.1088/1748-0221/12/10/P10003, arXiv:1706.04965.

[41] CMS Collaboration, "Performance of reconstruction and identification of τ leptons decaying to hadrons and ν_τ in pp collisions at $\sqrt{s} = 13$ TeV", *JINST* **13** (2018) P10005, doi:10.1088/1748-0221/13/10/P10005, arXiv:1809.02816.

[42] CMS Collaboration, "Jet energy scale and resolution in the CMS experiment in pp collisions at 8 TeV", *JINST* **12** (2017) P02014, doi:10.1088/1748-0221/12/02/P02014, arXiv:1607.03663.

[43] CMS Collaboration, "Performance of missing transverse momentum reconstruction in proton-proton collisions at $\sqrt{s} = 13$ TeV using the CMS detector", *JINST* **14** (2019) P07004, doi:10.1088/1748-0221/14/07/P07004, arXiv:1903.06078.

[44] CMS Collaboration, "Precision luminosity measurement in proton-proton collisions at $\sqrt{s} = 13$ TeV in 2015 and 2016 at CMS", *Eur. Phys. J. C* **81** (2021) 800, doi:10.1140/epjc/s10052-021-09538-2, arXiv:2104.01927.

[45] CMS Collaboration, "CMS luminosity measurement for the 2017 data-taking period at $\sqrt{s} = 13$ TeV", CMS Physics Analysis Summary CMS-PAS-LUM-17-004, 2018.

[46] CMS Collaboration, "CMS luminosity measurement for the 2018 data-taking period at $\sqrt{s}$ = 13 TeV", CMS Physics Analysis Summary CMS-PAS-LUM-18-002, 2019.

[47] CMS Collaboration, "The CMS experiment at the CERN LHC", *JINST* **3** (2008) S08004, doi:10.1088/1748-0221/3/08/S08004.

[48] C. Oleari, "The POWHEG-BOX", *Nucl. Phys. B Proc. Suppl.* **205-206** (2010) 36, doi:10.1016/j.nuclphysbps.2010.08.016, arXiv:1007.3893.

[49] J. Alwall et al., "The automated computation of tree-level and next-to-leading order differential cross sections, and their matching to parton shower simulations", *JHEP* **07** (2014) 079, doi:10.1007/JHEP07(2014)079, arXiv:1405.0301.

[50] T. Sjöstrand et al., "An introduction to PYTHIA 8.2", *Comput. Phys. Commun.* **191** (2015) 159, doi:10.1016/j.cpc.2015.01.024, arXiv:1410.3012.

[51] CMS Collaboration, "Extraction and validation of a new set of CMS PYTHIA8 tunes from underlying-event measurements", *Eur. Phys. J. C* **80** (2020) 4, doi:10.1140/epjc/s10052-019-7499-4, arXiv:1903.12179.

[52] GEANT4 Collaboration, "GEANT4 — a simulation toolkit", *Nucl. Instrum. Meth. A* **506** (2003) 250, doi:10.1016/S0168-9002(03)01368-8.

[53] NNPDF Collaboration, "Parton distributions from high-precision collider data", *Eur. Phys. J. C* **77** (2017) 663, doi:10.1140/epjc/s10052-017-5199-5, arXiv:1706.00428.

[54] H. B. Hartanto, B. Jager, L. Reina, and D. Wackeroth, "Higgs boson production in association with top quarks in the POWHEG BOX", *Phys. Rev. D* **91** (2015) 094003, doi:10.1103/PhysRevD.91.094003, arXiv:1501.04498.

[55] P. Nason and C. Oleari, "NLO Higgs boson production via vector-boson fusion matched with shower in POWHEG", *JHEP* **02** (2010) 037, doi:10.1007/JHEP02(2010)037, arXiv:0911.5299.

[56] G. Luisoni, P. Nason, C. Oleari, and F. Tramontano, "$HW^{\pm}/HZ + 0$ and 1 jet at NLO with the POWHEG BOX interfaced to GoSam and their merging within MiNLO", *JHEP* **10** (2013) 083, doi:10.1007/JHEP10(2013)083, arXiv:1306.2542.

[57] E. Bagnaschi, G. Degrassi, P. Slavich, and A. Vicini, "Higgs production via gluon fusion in the POWHEG approach in the SM and in the MSSM", *JHEP* **02** (2012) 088, doi:10.1007/JHEP02(2012)088, arXiv:1111.2854.

[58] LHC Higgs Cross Section Working Group, "Handbook of LHC Higgs cross sections: 4. deciphering the nature of the Higgs sector", CERN Report CERN-2017-002-M, 2016. doi:10.23731/CYRM-2017-002, arXiv:1610.07922.

[59] R. Frederix and S. Frixione, "Merging meets matching in MC@NLO", *JHEP* **12** (2012) 061, doi:10.1007/JHEP12(2012)061, arXiv:1209.6215.

[60] S. Zanoli et al., "Next-to-next-to-leading order event generation for VH production with $H \to b\bar{b}$ decay", *JHEP* **07** (2022) 008, doi:10.1007/JHEP07(2022)008, arXiv:2112.04168.

[61] M. L. Mangano, M. Moretti, F. Piccinini, and M. Treccani, "Matching matrix elements and shower evolution for top-quark production in hadronic collisions", *JHEP* **01** (2007) 013, doi:10.1088/1126-6708/2007/01/013, arXiv:hep-ph/0611129.

[62] J. M. Campbell, R. K. Ellis, P. Nason, and E. Re, "Top-pair production and decay at NLO matched with parton showers", *JHEP* **04** (2015) 114, doi:10.1007/JHEP04(2015)114, arXiv:1412.1828.

[63] S. Alioli, P. Nason, C. Oleari, and E. Re, "NLO single-top production matched with shower in POWHEG: s- and t-channel contributions", *JHEP* **09** (2009) 111, doi:10.1088/1126-6708/2009/09/111, arXiv:0907.4076. [Erratum: doi:10.1007/JHEP02(2010)011].

[64] E. Re, "Single-top Wt-channel production matched with parton showers using the POWHEG method", *Eur. Phys. J. C* **71** (2011) 1547, doi:10.1140/epjc/s10052-011-1547-z, arXiv:1009.2450.

[65] M. Czakon et al., "Top-pair production at the LHC through NNLO QCD and NLO EW", *JHEP* **10** (2017) 186, doi:10.1007/JHEP10(2017)186, arXiv:1705.04105.

[66] P. Artoisenet, R. Frederix, O. Mattelaer, and R. Rietkerk, "Automatic spin-entangled decays of heavy resonances in monte carlo simulations", *JHEP* **03** (2013) 015, doi:10.1007/JHEP03(2013)015, arXiv:1212.3460.

[67] T. Melia, P. Nason, R. Rontsch, and G. Zanderighi, "W^+W^-, WZ and ZZ production in the POWHEG BOX", *JHEP* **11** (2011) 078, doi:10.1007/JHEP11(2011)078, arXiv:1107.5051.

[68] M. Cacciari and G. P. Salam, "Pileup subtraction using jet areas", *Phys. Lett. B* **659** (2008) 119, doi:10.1016/j.physletb.2007.09.077, arXiv:0707.1378.

[69] CMS Collaboration, "Technical proposal for the phase-II upgrade of the compact muon solenoid", CMS Technical Proposal CERN-LHCC-2015-010, CMS-TDR-15-02, 2015.

[70] M. Cacciari, G. P. Salam, and G. Soyez, "The anti-k_T jet clustering algorithm", *JHEP* **04** (2008) 063, doi:10.1088/1126-6708/2008/04/063, arXiv:0802.1189.

[71] M. Cacciari, G. P. Salam, and G. Soyez, "Fastjet user manual", *Eur. Phys. J. C* **72** (2012) 1896, doi:10.1140/epjc/s10052-012-1896-2, arXiv:1111.6097.

[72] CMS Collaboration, "Study of pileup removal algorithms for jets", CMS Physics Analysis Summary CMS-PAS-JME-14-001, 2014.

[73] CMS Collaboration, "Identification of heavy-flavour jets with the CMS detector in pp collisions at 13 TeV", *JINST* **13** (2018) P05011, doi:10.1088/1748-0221/13/05/P05011, arXiv:1712.07158.

[74] CMS Collaboration, "Pileup mitigation at CMS in 13 TeV data", *JINST* **15** (2020) P09018, doi:10.1088/1748-0221/15/09/P09018, arXiv:2003.00503.

[75] D. Bertolini, P. Harris, M. Low, and N. Tran, "Pileup per particle identification", *JHEP* **10** (2014) 059, doi:10.1007/JHEP10(2014)059, arXiv:1407.6013.

[76] A. J. Larkoski, S. Marzani, G. Soyez, and J. Thaler, "Soft drop", *JHEP* **05** (2014) 146, doi:10.1007/JHEP05(2014)146, arXiv:1402.2657.

[77] M. Dasgupta, A. Fregoso, S. Marzani, and G. P. Salam, "Towards an understanding of jet substructure", *JHEP* **09** (2013) 029, doi:10.1007/JHEP09(2013)029, arXiv:1307.0007.

[78] J. M. Butterworth, A. R. Davison, M. Rubin, and G. P. Salam, "Jet substructure as a new Higgs search channel at the LHC", *Phys. Rev. Lett.* **100** (2008) 242001, doi:10.1103/PhysRevLett.100.242001, arXiv:0802.2470.

[79] J. Thaler and K. Van Tilburg, "Identifying boosted objects with N-subjettiness", *JHEP* **03** (2011) 015, doi:10.1007/JHEP03(2011)015, arXiv:1011.2268.

[80] CMS Collaboration, "Identification of heavy, energetic, hadronically decaying particles using machine-learning techniques", *JINST* **15** (2020) P06005, doi:10.1088/1748-0221/15/06/P06005, arXiv:2004.08262.

[81] G. Cowan, K. Cranmer, E. Gross, and O. Vitells, "Asymptotic formulae for likelihood-based tests of new physics", *Eur. Phys. J. C* **71** (2011) 1554, doi:10.1140/epjc/s10052-011-1554-0, arXiv:1007.1727. [Erratum: doi:10.1140/epjc/s10052-013-2501-z].

[82] T. Sakuma, H. Flächer, and D. Smith, "Alternative angular variables for suppression of QCD multijet events in new physics searches with missing transverse momentum at the LHC", 2018. arXiv:1803.07942.

[83] CMS Collaboration, "Performance of electron reconstruction and selection with the CMS detector in proton-proton collisions at $\sqrt{s} = 8$ TeV", *JINST* **10** (2015) P06005, doi:10.1088/1748-0221/10/06/P06005, arXiv:1502.02701.

[84] J. M. Lindert, S. Pozzorini, R. Boughezal et al., "Precise predictions for $V+$ jets dark matter backgrounds", *Eur. Phys. J. C* **77** (2017) 829, doi:10.1140/epjc/s10052-017-5389-1, arXiv:1705.04664.

[85] CMS Collaboration, "Precise determination of the mass of the Higgs boson and tests of compatibility of its couplings with the standard model predictions using proton collisions at 7 and 8 TeV", *Eur. Phys. J. C* **75** (2015) 212, doi:10.1140/epjc/s10052-015-3351-7, arXiv:1412.8662.

[86] ATLAS and CMS Collaborations, and LHC Higgs Combination Group, "Procedure for the LHC Higgs boson search combination in summer 2011", Technical report CMS-NOTE-2011-005, ATL-PHYS-PUB-2011-11, 2011.

[87] A. L. Read, "Presentation of search results: The CL_s technique", *J. Phys. G* **28** (2002) 2693, doi:10.1088/0954-3899/28/10/313.

[88] T. Junk, "Confidence level computation for combining searches with small statistics", *Nucl. Instrum. Meth. A* **434** (1999) 435, doi:10.1016/S0168-9002(99)00498-2, arXiv:hep-ex/9902006.

[89] CMS Collaboration, "Searches for invisible decays of the Higgs boson in pp collisions at $\sqrt{s} = 7$, 8, and 13 TeV", *JHEP* **02** (2017) 135, doi:10.1007/JHEP02(2017)135, arXiv:1610.09218.

[90] CMS Collaboration, "Search for invisible decays of Higgs bosons in the vector boson fusion and associated ZH production modes", *Eur. Phys. J. C* **74** (2014) 2980, doi:10.1140/epjc/s10052-014-2980-6, arXiv:1404.1344.

[91] CMS Collaboration, "Search for dark matter in proton-proton collisions at 8 TeV with missing transverse momentum and vector boson tagged jets", *JHEP* **12** (2016) 083, doi:10.1007/JHEP12(2016)083, arXiv:1607.05764. [Erratum: doi:10.1007/JHEP08(2017)035].

[92] S. Baker and R. D. Cousins, "Clarification of the use of chi square and likelihood functions in fits to histograms", *Nucl. Instrum. Meth.* **221** (1984) 437, doi:10.1016/0167-5087(84)90016-4.

[93] HEPData record for this analysis, 2023. doi:10.17182/hepdata.137761.

[94] M. Zaazoua, L. Truong, K. A. Assamagan, and F. Fassi, "Higgs portal vector dark matter interpretation: Review of effective field theory approach and ultraviolet complete models", *LHEP* **2022** (2022) 270, doi:10.31526/lhep.2022.270, arXiv:2107.01252.

[95] CRESST Collaboration, "First results from the CRESST-III low-mass dark matter program", *Phys. Rev. D* **100** (2019) 102002, doi:10.1103/PhysRevD.100.102002, arXiv:1904.00498.

[96] DarkSide-50 Collaboration, "Search for low-mass dark matter WIMPs with 12 ton-day exposure of DarkSide-50", 2022. arXiv:2207.11966.

[97] PandaX Collaboration, "A first search for solar ^{8}B neutrino in the PandaX-4T experiment using neutrino-nucleus coherent scattering", 2022. arXiv:2207.04883.

[98] LZ Collaboration, "First dark matter search results from the LUX-ZEPLIN (LZ) experiment", 2022. arXiv:2207.03764.

[99] R. D. Young and A. W. Thomas, "Octet baryon masses and sigma terms from an SU(3) chiral extrapolation", *Phys. Rev. D* **81** (2010) 014503, doi:10.1103/PhysRevD.81.014503, arXiv:0901.3310.

[100] MILC Collaboration, "The strange quark condensate in the nucleon in 2+1 flavor QCD", *Phys. Rev. Lett.* **103** (2009) 122002, doi:10.1103/PhysRevLett.103.122002, arXiv:0905.2432.

[101] LHC Higgs Cross Section Working Group, "Handbook of LHC Higgs cross sections: 3. Higgs properties", Technical report, 2013. doi:10.5170/CERN-2013-004, arXiv:1307.1347.